Spring 2011

Uncertainty quantification integrated to computational fluid dynamic modeling of synthetic jet actuators

Srikanth Adya

Department:

UNCERTAINTY QUANTIFICATION INTEGRATED TO COMPUTATIONAL FLUID DYNAMIC MODELING OF SYNTHETIC JET ACTUATORS

by

SRIKANTH ADYA

A THESIS

Presented to the Faculty of the Graduate School of the

MISSOURI UNIVERSITY OF SCIENCE AND TECHNOLOGY

In Partial Fulfillment of the Requirements for the Degree

MASTER OF SCIENCE IN AEROSPACE ENGINEERING

2011

Approved by

Serhat Hosder, Advisor
Fathi Finaish
Xiaoping Du

ABSTRACT

The Point Collocation Non-Intrusive Polynomial Chaos (NIPC) method was applied to a stochastic synthetic jet actuator problem to demonstrate the integration of computationally efficient uncertainty quantification to the high-fidelity CFD modeling of Synthetic Jet Actuators. The uncertainty quantification approach was first implemented in two stochastic model problem cases for the prediction of peak exit plane velocity using a Fluid Dynamic Based analytical model of the Synthetic Jet Actuator, which is computationally less expensive than CFD simulations. The NIPC results were compared with direct Monte Carlo sampling results. To demonstrate the efficient uncertainty quantification in CFD modeling of synthetic jet actuators, a test case, Case 1(synthetic jet issuing into quiescent air),was selected from the CFD-Val2004 workshop. In the stochastic CFD problem, the NIPC method was used to quantify the uncertainty in the long-time averaged u and v-velocities at several locations in the flow field, due to the uncertainty in the amplitude and frequency of the oscillation of the piezo-electric membrane. Fifth order NIPC expansions were used to obtain the uncertainty information which showed that the variation in the v-velocity is high in the region directly above the jet slot and the variation in the u-velocity is maximum in the region immediately adjacent to the slot. Even with a ten percent variation in the amplitude and frequency, the long-time averaged u and v-velocity profiles could not match the experimental measurements at $y = 0.1mm$ above the slot, indicating that the discrepancy may be due to other uncertainty sources in CFD or measurement errors. A global sensitivity analysis using linear regression approach indicated that the frequency had a stronger contribution to the overall uncertainty in the long-time averaged flow field velocity for the range of input uncertainties considered in this study. Overall, the results obtained in this study showed the potential of Non-Intrusive Polynomial Chaos as an effective uncertainty quantification method for computationally expensive high-fidelity CFD simulations applied to the stochastic modeling of synthetic jet flow fields.

ACKNOWLEDGMENTS

I would like to convey my deepest and sincere gratitude to my advisor, Dr. Serhat Hosder, for his continuous guidance during my study and research at Missouri S&T. His perpetual energy and enthusiasm has been a great source of inspiration for me. I am also thankful to him for the financial assistance he has given me in the form of Research and Teaching Assistantships.

Special thanks to Dr.Rajnish N. Sharma and Dr. Louis N. Cattafesta for their help in realizing the model problem included in this work. I would also like to thank my committee members Dr. Fathi Finaish and Dr. Xiaoping Du for their constructive criticism and guidance.

Working along with Benjamin Bettis, Yi Zang and Daoru Han at the Computational Fluid Dynamics and Aerospace Design Lab has been a memorable experience. I would like to thank them for their support at every stage of this research work.

Last but not the least, I would like to thank my family and friends. Their constant encouragement and guidance kept me focused and motivated.

TABLE OF CONTENTS

Page

LIST OF ILLUSTRATIONS

LIST OF TABLES

NOMENCLATURE

Symbol	Description
$v(t)$	applied voltage in (V)
$F(t)$	driving force (N)
F	amplitude of the driving force (N)
$U(t)$	orifice flow velocity (m/s)
$p_i(t)$	cavity internal pressure (Pa)
A_0	orifice area (m^2)
A_w	wall area (m^2)
C_I	Inertia Coefficient
C_{Leff}	effective loss coefficient
c_w	diaphragm damping coefficient
c_a	added diaphragm damping co-efficient
c_{wt}	c_a+c_w
D_a	effective acoustic piezo-electric co-efficient
d_0	orifice diameter (m)
d_w	diaphragm/wall diameter (m)
f_h	hemholtz frequency (Hz)
f_w	diaphragm/wall natural frequency (Hz)
k_w	diaphragm/wall stiffness (N/m)
l_e	effective length of air slug (m)

m_w	diaphragm/wall mass (kg)
m_a	added diaphragm/wall mass (kg)
m_{wt}	m_a+m_w
p_i	gauge internal pressure (Pa)
P_0	ambient pressure (Pa)
ΔV	volume displaced by the diaphragm (m^3)
x_w	wall displacement (m)
ω	$2\pi f$ (rad/s)
ω_w	$2\pi f_w$ (rad/s)
ω_h	$2\pi f_h$ (rad/s)
U_S	speed of sound (m/s)
u_i	velocity component where $(i = 1, 2, 3)$
$\bar{u}_i$	mean component of the velocity
u_i'	fluctuating component of the velocity
μ_t	turbulent viscosity
k	turbulence kinetic energy
ω	specific dissipation rate
$\tilde{G}_k$	generation of turbulence kinetic energy
G_ω	generation of ω
Γ_k	diffusivity of k
Γ_ω	diffusivity of ω
Y_k	dissipation of k

Y_ω	dissipation of ω
D_ω	cross-dissipation term
σ_k	turbulent Prandtl number for k
σ_ω	turbulent Prandtl number for ω
S	strain rate magnitude
D	displacement of the membrane (m)
a_0	amplitude of displacement (m)
f	frequency of oscillation (Hz)
U	velocity of the membrane (m/s)
A_0	amplitude of membrane velocity (m/s)

1. INTRODUCTION

In this section a brief introduction is presented on the use of synthetic jet actuator for flow control, their working principle and some previous studies that focused on computational modeling of synthetic jet actuators. This is followed by a brief discussion on the need for integrating uncertainty quantification, in particular, the Non-Intrusive Polynomial Chaos approach, with high-fidelity CFD modeling of synthetic jet actuators. Finally, the contributions of the current study and the general outline of this manuscript are listed towards the end of this section.

1.1. SYNTHETIC JET ACTUATORS

Flow control involves active or passive devices that produce beneficial changes in wall bounded or free shear flows. Effective flow control can be employed to either delay or advance transition, suppress or improve turbulence or prevent or provoke flow separation depending on the application and the associated flow field. The potential benefits of realizing efficient flow control include drag reduction, lift enhancement, better mixing and noise suppression to name a few[1].

Among the flow control devices, synthetic jet actuators are one of the most-frequently studied configurations since they are highly promising in terms of realizing actual flow control system on an aircraft. In a typical synthetic jet actuator configuration, the jet is produced by a moving membrane that is built into the wall of the cavity. This jet is ejected out through an orifice that can be directly mounted on the control surface. The simplicity of the design obviates the need for complex ducting and packaging and hence a more attractive solution.

Unique to synthetic jets, is also the fact that, they are formed by the working fluid in the flow system in which they are employed. This results in addition of momentum to the system without adding any mass, hence the name zero-net-mass-flux jets. During the ejection half of the membrane motion, for a two-dimensional

orifice, the flow separates at the sharp edges of the orifice and rolls into a pair of counter rotating vortices. These vortical structures then move away from the orifice under their own self induced velocity. In the presence of a cross-flow, these vortex pairs convect downstream entraining fluid from the free stream, resulting in favorable local displacement of the streamlines and pressure distribution changes at these regions.

In recent years there have been a number of experimental and numerical investigations of the pulsating synthetic jets. A good reference of these works can be found in a review paper by Glezer and Amitay[2]. Among CFD studies involving synthetic jets, Rizzetta et.al [3] have investigated numerically the flow characteristics of a synthetic jet issuing into quiescent air. They noted that the internal geometry of the actuator had a huge influence on the jet profiles at the exit. Mittal et al. [4] modeled numerically an isolated synthetic jet with a flat plate boundary layer and descried the dynamics of the synthetic jet in the presence of external cross-flow. They also found that the synthetic jet was capable of altering the effective shape of the body by forming a recirculation bubble. Cui et.al [5] performed 2-D simulations of a synthetic jet in turbulent boundary layer. They used an unsteady RANS solver with Spalart-Allmaras turbulent model and compared their results with experiments. Although the results compared well qualitatively, there were significant quantitative difference between the CFD and experimental results.

1.2. MOTIVATION FOR UNCERTAINTY QUANTIFICATION

The high-fidelity Computational Fluid Dynamics (CFD) simulations that can accurately predict the synthetic jet behavior are important to understand the flow physics and be able to design robust actuators that can work efficiently in various operating conditions. In order to assess the state-of-the-art CFD modeling of these actuators, a validation workshop for synthetic jets and turbulent separation control (CFDVAL2004)[6] was held at NASA Langley Research Center in 2004. The workshop focused on numerical formulation of a number of synthetic jet configurations, which were selected as test cases for participants. Summary of the workshop results can be

found in Rumsey et al [7]. One of the conclusions of the workshop was that, due to the uncertainty involved in modeling the unsteady boundary conditions, CFD was only able to qualitatively predict the flow physics but failed to consistently achieve quantitative predictions [8]. Several parameters such as the amplitude and angular frequency of oscillation of the diaphragm, the geometric dimensions such as width and height of the cavity and the slot, characterize the time dependent diaphragm deflection and the cavity flow. In real life applications, the performance of a synthetic jet actuator will be affected by the uncertainties in these parameters as well as the variation in the operating conditions such as the free stream velocity of the cross flow. In addition, the uncertainties in the physical models (i.e., turbulence models), boundary, and initial conditions used in CFD simulations will affect the accuracy of the results, which emphasizes the need for uncertainty quantification in numerical simulations.

1.3. OBJECTIVE OF THE CURRENT STUDY

The objective of the current study is the integration of uncertainty quantification (UQ) to the CFD modeling of synthetic jet actuators. The uncertainty information obtained for the selected output quantities of interest will be important for the assessment of the accuracy of the results and can be used in the robust and reliability based design of a synthetic jet actuator.

There have been several studies on the application of non-intrusive spectral techniques to quantify the uncertainty in CFD simulations ranging from low-order models to Large-Eddy Simulations (e.g., Lucor et. al. [9]). In a recent paper, Najm [10] gives a comprehensive review on the theory and application of polynomial chaos techniques for CFD simulations. A review on the application of non-intrusive polynomial chaos methods to fluid dynamics problems is given by Hosder and Walters [11].

An important aspect of the current study is to demonstrate the application of the Point-Collocation Non-Intrusive Polynomial Chaos (NIPC) Method to propagate the input uncertainties in the computational modeling of synthetic jet actuators. In

general the NIPC methods, which are based on spectral representation of the uncertainty, are computationally more efficient than the traditional Monte Carlo methods for stochastic fluid dynamic problems with moderate number of uncertain variables as shown in studies by Hosder et. al. ([11] and [12]) and can give highly accurate estimates of various uncertainty metrics. In addition, they treat the deterministic model (e.g. the CFD code) as a black box and the uncertainty information in the output is approximated with a polynomial expansion, which is constructed using a number of deterministic solutions, each corresponding to a sample point in a random space. Therefore, NIPC methods become a perfect candidate for the uncertainty quantification in the high-fidelity modeling of synthetic jet actuators, since these simulations require the numerical solution of viscous, turbulent, unsteady flow fields, which can be computationally expensive and complex.

1.4. CONTRIBUTIONS OF THE CURRENT STUDY

One of the main contributions of this research project is that, this was the first study to integrate uncertainty quantification to high-fidelity CFD modeling of synthetic jet actuators. The uncertainty metrics so obtained can be used for robust and/or reliability based design of synthetic jet actuators in future studies. The methodology used for uncertainty quantification in this work is highly efficient compared to conventional Monte Carlo methods. Hence this study serves an example for efficient uncertainty quantification using Non-Intrusive Polynomial Chaos approach in computationally expensive high-fidelity flow simulations.

1.5. THESIS OUTLINE

In this study, the uncertainty quantification approach is applied to a fluid dynamics based analytical model and the CFD modeling of the synthetic jet actuator. The test case (Case 1 used in the CFDVAL2004 workshop) was chosen for CFD modeling since sufficient experimental and numerical results were available. The following section describes the categorization of the types of uncertainties and explains

the Polynomial-Chaos method, in particular, the Non-Intrusive Polynomial-Chaos approach.

The third section describes the analytical formulation used to represent the synthetic jet actuator. The governing equations of this fluid-dynamics-based model is outlined. This section also describes the implementation of the uncertainty quantification approach. Since the analytical model is computationally inexpensive to evaluate, the results from the NIPC approach are compared with that from Monte Carlo simulation which serves as a validation for this approach.

The fourth section details the uncertainty quantification approach applied to computational modeling of the synthetic jet actuator. All details of the computational modeling as well as the stochastic CFD modeling is discussed in this section. The results of the uncertainty quantification are presented towards end of this section. Finally, Section five presents the relevant conclusions from the current study and the intended future work.

2. UNCERTAINTY QUANTIFICATION APPROACH

In this section, the methodology used to propagate and quantify the uncertainties in in the current study is presented. In particular, the Point-Collocation Non-Intrusive Polynomial Chaos method has been described in detail. Before discussing the NIPC method a brief introduction is presented on the categorization of the types of uncertainties followed by some basic insights into the Polynomial Chaos theory.

2.1. CHARACTERIZATION OF UNCERTAINTIES

Uncertainty based design methods require that the various uncertainties arising in the computational modeling be characterized and managed and the analysis and optimization methods incorporate these characterization. As discussed in Oberkampf et.al [13], uncertainties in computational simulations can be categorized into three main categories: (1) aleatory uncertainty, (2) epistemic uncertainty and (3) numerical error. Aleatory or parametric uncertainty is defined as "inherent variation associated with the physical system or the environment under consideration". These uncertainties can be attributed to the randomness associated with initial and boundary conditions imposed on the model. Depending on the application, there are several examples for aleatory uncertainties. In case of CFD modeling of synthetic jet actuator, some of the possible aleatory uncertainties could be, variation in the amplitude and frequency of the oscillating membrane, the free stream velocity of the cross-flow or the geometric tolerances. Aleatory uncertainties are generally represented mathematically as probability distributions if sufficient experimental data for estimating the statistical distribution are available. The common types of statistical distributions are uniform, normal(Gaussian), lognormal, etc. Since these uncertainties are always present in the model owing to the stochastic nature of the input parameters, these uncertainties are also called as irreducible uncertainties.

Epistemic uncertainty is defined as "any lack of knowledge or information in any phase or activity of the modeling process". Their source lies in the fact that there is incomplete information or incomplete knowledge available on some phase or activity of the modeling process. Unlike aleatory uncertainties, the epistemic uncertainties can reduce once enough knowledge or information becomes available. Hence this type of uncertainty is also referred to as reducible uncertainty. Also, another important distinction between epistemic and aleatory uncertainties is that the epistemic uncertainty cannot be represented using a statistical distribution due to lack of information or knowledge. Hence the common practice is to use intervals. An upper and lower bound is assigned to the uncertain variable based on experimental data or expert judgment. Since no statistical distribution can be assigned, all values within this range are assumed to have equal probability of occurrence.

Numerical error is defined as "a recognizable deficiency in any phase or activity of modeling and simulation that is not due to lack of knowledge." In most engineering scenarios mathematical models usually involve systems of non-linear partial differential equations (PDEs). The solution of these PDEs are associated with spatial and temporal discretization errors due to iterative convergence of approximation algorithms. It is very important to minimize the numerical errors in computational simulations since they can easily propagate through the simulation along with aleatory and epistemic uncertainties. Consequently one cannot estimate the individual contributions of the input uncertainties on the overall uncertainty of the output parameter of interest. In the current study, we focus on modeling and propagating only aleatory uncertainties.

2.2. BASICS OF POLYNOMIAL CHAOS

For the uncertainty quantification of synthetic jet actuator formulation, the Point-Collocation Non-Intrusive Polynomial Chaos (NIPC) [14] method was used to propagate the input uncertainty to the output quantities of interest. The Point Collocation NIPC is derived from polynomial chaos theory, which is based on the spectral

representation of the uncertainty. An important aspect of spectral representation of uncertainty is that one may decompose a random function (or variable) into separable deterministic and stochastic components. For example, for any random variable ($i.e., \alpha^*$) such as velocity, density or pressure in a stochastic fluid dynamics problem, we can write,

$$\alpha^*(\vec{x}, t, \vec{\xi}) \approx \sum_{j=0}^{P} \alpha_j(\vec{x}, t)\Psi_j(\vec{\xi}) \tag{1}$$

where $\alpha_j(\vec{x}, t)$ is the deterministic component and $\Psi_j(\vec{\xi})$ is the random basis function corresponding to the j^{th} mode. In the most general case, α^* can be a function of deterministic independent variable vector $\vec{x}$, time t, and the n-dimensional standard random variable vector $\vec{\xi} = (\xi_1, ..., \xi_n)$. In theory, the polynomial chaos expansion given by Equation 1, should include infinite number of terms, however in practice a discrete sum is taken over a number of output modes (or total number of terms, N_t) with

$$N_t = P + 1 = \frac{(n+p)!}{n!p!} \tag{2}$$

which is a function of the order of polynomial chaos (p) and the number of random dimensions (n). The basis functions used in the stochastic expansion given in Equation 1 are polynomials that are orthogonal with respect to a weight function over the support region of the input random variable vector. The basis function takes the form of multi-dimensional Hermite Polynomial to span the n-dimensional random space when the input uncertainty is Gaussian (normal), which was first used by Wiener[15] in his original work of polynomial chaos. To extend the application of the polynomial chaos theory to the propagation of continuous non-normal input uncertainty distributions, Xiu and Karniadakis[16] used a set of polynomials known as the Askey scheme to obtain the "Wiener-Askey Generalized Polynomial Chaos". The commonly used Hermite, Legendre, and Laguerre polynomials and the associated probability density functions (PDF) are listed in Table 2.1. The Legendre and Laguerre polynomials, which are among the polynomials included in the Askey scheme are optimal basis functions for bounded (uniform) and semi-bounded (exponential) input uncertainty

distributions respectively in terms of the convergence of the statistics. The optimal choice of the basis function is derived from the inner product weighting functions of the PDFs of the continuous input uncertainty distributions represented in their standard form. The constant multiplicative factor between the density function and the weight function originates from the fact that the integral of the PDF over the support range must be exactly one.

Table 2.1. Univariate Hermite, Legendre, and Laguerre polynomials and the associated continuous probability distributions.

Distribution	Density Function	Polynomial	Weight Function $p(\xi)$	Support Range (R)
Normal	$\frac{1}{\sqrt{2\pi}}e^{\frac{-\xi^2}{2}}$	Hermite $H_n(\xi)$	$e^{\frac{-\xi^2}{2}}$	$[-\infty,\infty]$
Uniform	$\frac{1}{2}$	Legendre $Le_n(\xi)$	1	$[-1,1]$
Exponential	$e^{-\xi}$	Laguerre $La_n(\xi)$	$e^{-\xi}$	$[0,\infty]$

The multivariate basis functions can be obtained from the product of univariate orthogonal polynomials (See Eldred et. al[17]). For example a multivariate Hermite polynomial can be calculated by

$$H_n(\xi_{i_1},...,\xi_{i_n}) = H_n(\vec{\xi}) = e^{\frac{1}{2}\vec{\xi}^T\vec{\xi}}(-1)^n\frac{\delta^n}{\delta\xi_{i_1}...\delta\xi_{i_n}}e^{-\frac{1}{2}\vec{\xi}^T\vec{\xi}} \tag{3}$$

which can also be obtained by the product of one-dimensional Hermite Polynomials $(\psi_{m_i^j}(\xi_i))$ with the use of a multi-index m_i^j as shown by Eldred *et. al* [**?**]:

$$H_n(\xi_{i_1},...,\xi_{i_n}) = \Psi_j(\vec{\xi}) = \prod_{i=1}^{n}\psi_{m_i^j}(\xi_i) \tag{4}$$

If the probability distribution of each random variable is different, then the optimal multivariate basis functions can be again obtained by the product of univariate orthogonal polynomials employing the optimal univariate polynomial at each random dimension. This approach requires that the input uncertainties are independent standard random variables, which also allows the calculation of the multivariate weight

functions by the product of univariate weight functions associated with the probability distribution at each random dimension. The detailed information on polynomial chaos expansions can be found in Walters and Huyse[18], Najm[10], and Hosder and Walters[12].

The objective of the stochastic methods based on polynomial chaos is to determine the coefficient of each term ($\alpha_j(\vec{x},t)$, $(j=0,1,..,P)$) in the Equation 1. Once the coefficients are known the statistics of the stochastic output at a spatial location and time can then be calculated using the coefficients of the basis functions. Hosder et al. [11] have shown that the mean of the random solution is given by

$$\bar{\alpha}^*(\vec{x},t) = E_{PC}\left[\alpha^*(\vec{x},t,\vec{\xi})\right] = \int_R \alpha^*(\vec{x},t,\vec{\xi})p(\vec{\xi})d\vec{\xi} = \alpha_0(\vec{x},t) \tag{5}$$

This means that the expected value(mean) of the output $\alpha^*(\vec{x},t,\vec{\xi})$ corresponds to the zeroth mode of the expansion. They also express the variance of the distribution as:

$$Var_{PC}\left[\alpha^*(\vec{x},t,\vec{\xi})\right] = \int_R \left(\alpha^*(\vec{x},t,\vec{\xi}) - \bar{\alpha}_0^*(\vec{x},t)\right)^2 p(\vec{\xi})d\vec{\xi} = \sum_{j=1}^{P}\left[\alpha_j^2(\vec{x},t) < \Psi_j^2 >\right] \tag{6}$$

Above two equations are based on the fact that $\langle\Psi_j\rangle = 0$ for $j > 0$ and $\langle\Psi_i\Psi_j\rangle = \left\langle\Psi_j^2\right\rangle \delta_{ij}$, where the inner product of $\Psi_i(\vec{\xi})$ and $\Psi_j(\vec{\xi})$ in the support region R is defined as

$$\left\langle \Psi_i(\vec{\xi})\Psi_j(\vec{\xi})\right\rangle = \int_R \Psi_i(\vec{\xi})\Psi_j(\vec{\xi})p(\vec{\xi})d\vec{\xi} \tag{7}$$

with $p(\vec{\xi})$ being the weight function.

To model the uncertainty propagation in computational simulations via polynomial chaos with an intrusive approach, all dependent variables and random parameters in the governing equations are replaced with their polynomial chaos expansions. Taking the inner product of the equations, (or projecting each equation onto j^{th} basis) yield $P+1$ times the number of deterministic equations which can be solved by the same numerical methods applied to the original deterministic system. Al-

though straightforward in theory, an intrusive formulation for complex problems can be relatively difficult, expensive, and time consuming to implement. To overcome such inconveniences associated with the intrusive approach, non-intrusive polynomial chaos formulations have been considered for uncertainty propagation.

2.3. POINT-COLLOCATION NON-INTRUSIVE POLYNOMIAL CHAOS

The Point-Collocation NIPC method starts with replacing the uncertain variables of interest with their polynomial expansions given by Equation 1. Then, $P+1$ vectors ($\vec{\xi_i} = \{\xi_1, \xi_2, ..., \xi_n\}_i$, $i = 0, 1, 2, ..., P$) are chosen in random space for a given PC expansion with $P+1$ modes and the deterministic code is evaluated at these points. With the left hand side of Equation (1) known from the solutions of deterministic evaluations at the chosen random points, a linear system of equations can be obtained:

$$\begin{pmatrix} \Psi_0(\vec{\xi_0}) & \Psi_1(\vec{\xi_0}) & \cdots & \Psi_P(\vec{\xi_0}) \\ \\ \Psi_0(\vec{\xi_1}) & \Psi_1(\vec{\xi_1}) & \cdots & \Psi_P(\vec{\xi_1}) \\ \vdots & \vdots & \ddots & \vdots \\ \Psi_0(\vec{\xi_P}) & \Psi_1(\vec{\xi_P}) & \cdots & \Psi_P(\vec{\xi_P}) \end{pmatrix} \begin{pmatrix} \alpha_0(\vec{x}, t) \\ \\ \alpha_1(\vec{x}, t) \\ \vdots \\ \alpha_P(\vec{x}, t) \end{pmatrix} = \begin{pmatrix} \alpha^*(\vec{x}, t, \vec{\xi_0}) \\ \\ \alpha^*(\vec{x}, t, \vec{\xi_1}) \\ \vdots \\ \alpha^*(\vec{x}, t, \vec{\xi_P}) \end{pmatrix} \tag{8}$$

The spectral modes $\alpha_j(\vec{x}, t)$ of the random variable, $\alpha^*(\vec{x}, t, \vec{\xi})$, are obtained by solving the linear system of equations given above. The solution of linear problem given by Equation 8 requires $P+1$ deterministic function evaluations. If more than $P+1$ samples are chosen, then the over-determined system of equations can be solved using a Least Squares approach. Hosder et al.[19] investigated this option by increasing the number of collocation points in a systematic way through the introduction of a parameter n_{ps} defined as

$$n_{ps} = \frac{number\ of\ samples}{(P+1)} \tag{9}$$

Their results on model stochastic problems showed that using a number of collocation points that is twice more than the minimum number required (n_p=2) gives a better approximation to the statistics at each polynomial degree. The Point-Collocation NIPC has the advantage of flexibility on the selection of collocation points in random space (i.e., random, Latin HyperCube, Hammersley, importance sampling etc.) and possible re-use of collocation points for higher-order polynomial construction (i.e., selection of collocation points with incremental Latin Hypercube sampling). With the proper selection of collocation points, it has been shown that Point-Collocation NIPC can produce highly accurate stochastic response surfaces with computational efficiency in various stochastic fluid dynamics problems[12, 19].

2.4. IMPLEMENTATION OF POINT-COLLOCATION NIPC IN THE CURRENT STUDY

The above described method has been applied for uncertainty quantification of the output maximum velocity in the case of the model problem (i.e, Fluid Dynamics Based (FDB) formulation of the synthetic jet actuator) and the long-time averaged velocity components in case of the CFD formulation. Therefore, to construct the polynomial chaos expansions via Point-Collocation NIPC, the FDB model as well as the deterministic CFD code were evaluated with the input corresponding to the collocation points sampled from the random space of input uncertain variable vector. For example, to construct a 5^{th} degree polynomial chaos expansion with two uncertain input variables (Equation 2) with a oversampling ratio of 2 (Equation 9), a total number of 42 collocation points were required. Hence the model and the deterministic CFD code were evaluated at these 42 locations in the sample space. In case of the CFD simulations, each time dependent CFD simulation was run until the periodicity in the output quantity of interest was achieved. The long-time averaged or phase averaged value of the output quantity was calculated from each CFD simulation. Then using these values (the RHS vector in Equation 8), the coefficients of the polynomial chaos expansion were obtained following the procedure described above. Since the approach is non-intrusive, the deterministic solver can be treated as a black-box.

Hence, the outputs from Fluent were exported as data files and the co-efficients of the polynomial chaos expansion were evaluated externally using a MATLAB routine, that we developed, without the need to integrate this routine with the CFD solver. From the polynomial chaos expansions, various statistics such as the mean, standard deviation, the cumulative density function (CDF), and 95% confidence interval for the output quantity of interest which can be a point quantity (pressure, velocity, vorticity, etc.) anywhere in the flow field or an integrated flow quantity (such as the lift and drag coefficients) can be calculated (See Hosder at al.[11, 12] for details). It is also important to note that for a moderate number of input uncertainties, non-intrusive polynomial chaos methods are computationally more efficient than the traditional sampling-based methods such as Monte Carlo for uncertainty propagation.

The Point Collocation NIPC method has been previously applied to various stochastic fluid dynamics problems including low speed viscous flows, supersonic expansions, transonic 3-D wing flow fields and hypersonic re-entry vehicle configurations for uncertainty quantification (See Hosder et al, [12],[20] and Bettis et.al [21] for details). The stochastic results of these studies have shown good agreement with Latin Hypercube Monte-Carlo results of the same cases, which were obtained for the validation of the Point-Collocation NIPC method. The same procedure has been followed in the current study to validate the NIPC method with direct Monte Carlo sampling for the two model problem cases.

3. UNCERTAINTY QUANTIFICATION APPLIED TO MODEL PROBLEM

Before applying the Point-Collocation NIPC approach to the high fidelity CFD problem, the method was first applied to two model problem cases which included the prediction of the orifice exit plane centerline velocity . The first case was application of the Fluid-Dynamics-Based Model to compare its predictions with the results of Case 1 from Gallas et.al [22]. Second case was the extension of the Fluid-Dynamics-Based Model to predict the orifice exit plane centerline velocity for the experimental setup used in Case 1 of CFDVal2004 workshop. It should be noted here that this same case was used for stochastic CFD modeling which has be discussed in detail in chapter four. Also, in all the above mentioned cases the synthetic jet issued into quiescent air medium. Analytical models, unlike CFD simulations, are very economical to run several thousand simulations. Hence, these cases were used to compare the results from NIPC approach with that from Monte Carlo.

3.1. MODEL DESCRIPTION

The model by Sharma [23] is based on the laws of fluid dynamics,(unlike the Lumped Element Model, which uses electrical circuit analogy) to represent the synthetic jet flow and hence the name Fluid-Dynamics-Based Model (FDB). Along with predicting the velocity on the orifice exit plane it also estimates the cavity internal pressure and the phase relationship between the different variables [23]-[24]. The synthetic jet is produced by a moving membrane that is built into the wall of a cavity as shown in Figure 3.1. This membrane is a piezoelectric membrane. The motion of the membrane can be controlled by the application of an input voltage.

The model develops a relation between the applied input voltage $v(t)$, thus the applied driving force $F(t)$, to the orifice flow velocity $U(t)$ and the cavity internal pressure $p_i(t)$. For simplicity the motion of the membrane was assumed to be piston type and was modeled as a mass-damper-stiffness system having a mass m_w, damping

co-efficient c_w and a stiffness k_w. An additional mass term m_a is added for light weight membranes. Also an aerodynamic-acoustic damping corresponding to $c_a\dot{x}_w$ is also expected to act on the system. When actuated the guage pressure inside the cavity fluctuates about a mean value. The membrane oscillates against this fluctuating pressure under the influence of the applied driving force. The membrane dynamics under these forces can be written as:

$$\ddot{x}_w + 2\zeta_w\omega_w\dot{x}_w + \omega_w^2 x_w = \frac{F}{m_{wt}} - \frac{p_i A_w}{m_{wt}} \tag{10}$$

This wall oscillation causes the air inside the cavity to undergo alternative compression and expansion causing an oscillatory flow through the orifice. The continuity equation in that case can be written as:

$$V_0(dp_i/dt)/(\gamma P_0) - A_w\dot{x}_w = -A_0 U \tag{11}$$

Applying the unsteady form of the Bernoulli's equation between a point inside the cavity and the vena-contracta leads to

$$p_i = C_{Leff}\frac{1}{2}\rho_a|U|U + \rho_a l_e\,(dU/dt) \tag{12}$$

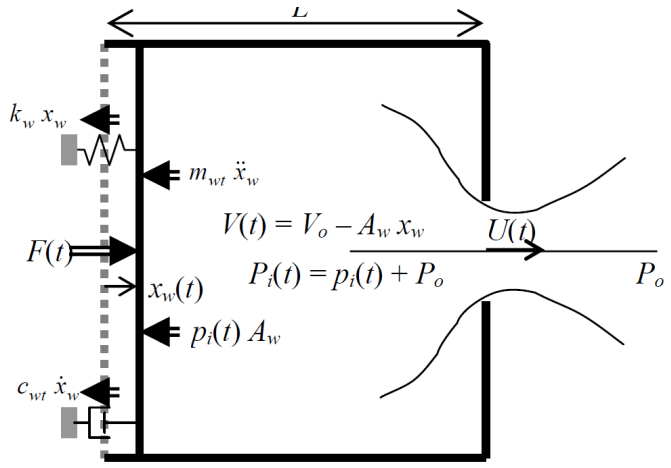

Figure 3.1. Schematic of the Synthetic Jet Actuator used in FDB formulation [23]

Eliminating the orifice flow velocity U first and then the internal pressure p_i from Equation 12 will result in two separate equations defining the dynamics of the internal pressure and dynamics of the mean orifice flow velocity expressed as below

$$\ddot{p}_i + V_0 K/\left(2\gamma A_0 P_0 l_e\right)|\dot{p}_i - (\gamma A_w P_0/V_0)\dot{x}_w|(\dot{p}_i - (\gamma A_w P_0/V_0)\dot{x}_i) + \omega_h^2 p_i = (\gamma A_w P_0/V_0)\ddot{x}_w + \omega_h^2 p_e \tag{13}$$

$$\ddot{U} + (K/l_e)|U|\dot{U} + \omega_w^2 p_i = (A_w/A_0)\omega_h^2 \dot{x}_w \tag{14}$$

A more detailed discussion on the derivation of these equations can be found in references [23], [25] and [24]. The Equations (10), (13) and (14) represent a coupled mechanical - Hemholtz resonator system with two degrees of freedom. These coupled equations form the synthetic jet actuator model. A forth order Runge-Kutta scheme was used to solve this system of non-linear ordinary differential equations. A built in MATLAB function, ODE45, was used to implement this scheme. ODE45 is set up to handle only first-order equations and so a method was needed to convert this second order equation into first-order equations which are equivalent. The conversion was accomplished through a technique called "reduction of order" as shown below:

$$\dot{p}_i = P \tag{15}$$

$$\dot{U} = T \tag{16}$$

$$\dot{P} + V_0 K/\left(2\gamma A_0 P_0 l_e\right)|P - (\gamma A_w P_0/V_0)\dot{x}_w|(P - (\gamma A_w P_0/V_0)\dot{x}_i) + \omega_h^2 p_i = (\gamma A_w P_0/V_0)\ddot{x}_w + \omega_h^2 p_e \tag{17}$$

$$\dot{T} + (K/l_e)|U|T + \omega_w^2 p_i = (A_w/A_0)\omega_h^2 \dot{x}_w \tag{18}$$

These four equations along with Equation 10, needs to be solved simultaneously to obtain the flow field parameters (internal pressure, exit plane velocity and membrane displacement). The input to the model is a sinusoidal force on the diaphragm. From the available amplitude of the voltage and the acoustic piezoelectric co-efficient D_a of the diaphragm, the maximum driving force F available at the membrane needs

to be estimated. For this the magnitude of the volume displaced was obtained as $\Delta V = D_a V$. The volume displacement so obtained was equated to the equivalent volume displacement i.e. $\Delta V = A_w x_w$. Dividing both sides by the area of the membrane gave the amplitude of the membrane displacement. The driving force was then calculated by combining this displacement with the stiffness of the diaphragm k_w. The solution was advanced in time by initializing all variables to zero and by a proper selection of the time step based on the frequency.

3.2. APPLICATION OF MODEL PROBLEM TO DETERMINISTIC SYNTHETIC JET CASES

3.2.1. Case 1. Case 1 corresponds to the first case studied by Gallas et.al [22] in their LEM model validation. Sharma has used this case to validate the fluid-dynamics-based model in [23], [25] and [24]. The same case was used here to validate the reproduction of the FBD model for this study. The Figures 3.2(a)and 3.2(b) compare the LEM prediction and the experimental measurements of the orifice exit plane velocity with the FDB model as a function of operating frequency. There is a good agreement between the present model and the experiment, except in the mid frequency range, where the model over predicts the maximum velocity. A similar trend was found in Sharma [23].

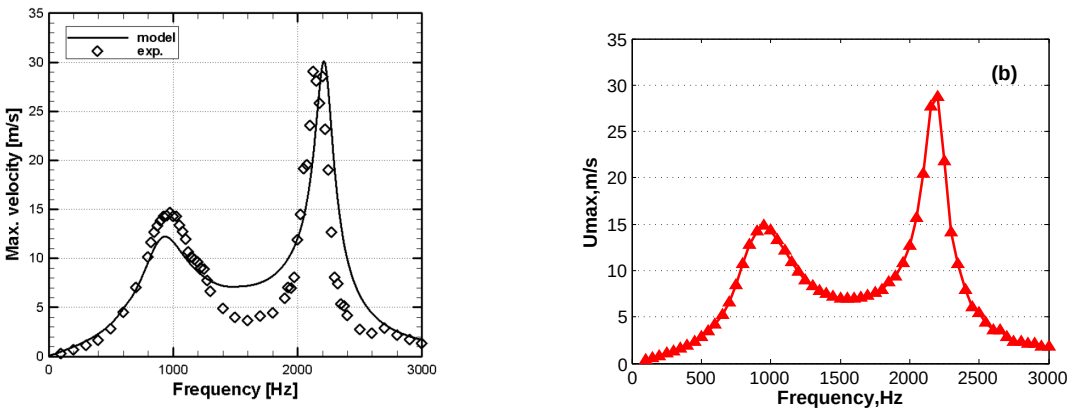

(a) LEM and experimental results

(b) FDB Prediction

Figure 3.2. Comparison LEM and FDB prediction for Case 1 from Gallas et.al [22]

Table 3.1 lists all the properties of the piezoelectric-driven synthetic jet actuator setup of Case 1 from Gallas et.al [22] and [26].

Table 3.1. Properties of Piezoelectric-driven synthetic jet actuator from [22] and [26]

		Case I
Brass Shim	Density (kg/m^3)	8700
	Thickness (mm)	0.2
	Diameter (mm)	23.5
Piezoceramic	Density (kg/m^3)	7700
	Thickness (mm)	0.11
	Diameter (mm)	20.5
Diaphragm	Compliance ($s^2.m^4/kg$)	6.53E-13
	Acoustic Mass (kg/m^4)	8.15E03
	Acoustic piezoelectric coefficientD_a (m^3/V)	5.53E-11
	Mechanical damping ratio	0.03
	Natural frequency Hz	2114
Cavity	Volume (m^3)	2.50E-06
	Equivalent cylindrical diameter (mm)	23.5
	Equivalent cylindrical length (mm)	5.76
Orifice	Diameter (mm)	1.65
	Length (mm)	1.65
	Effective loss coefficient	0.78
	Inertia coefficient	0.705
	Helmholtz frequency (Hz)	977
Forcing	Voltage amplitude (V)	25
	Force amplitude (N)	0.9925

3.2.2. Case 2. Case 2 corresponds to the first case studied at the CFDVal2004 workshop [7]. The FDB model was extended to predict the maximum output velocity at the orifice exit plane of the synthetic jet actuator. Table 3.2 lists all the properties of the piezoelectric-driven synthetic jet actuator setup of Case 1 from CFDVal2004 workshop [7]. Since the FDB model was not applied to this case before, the validity of the model was established by comparing the predictions with that from LEM model. The Figures 3.3(a)and 3.3(b) compare the LEM prediction of the orifice exit plane velocity with the FDB model as a function of operating frequency. Note that the output is normalized with the experimentally measured exit plane velocity.

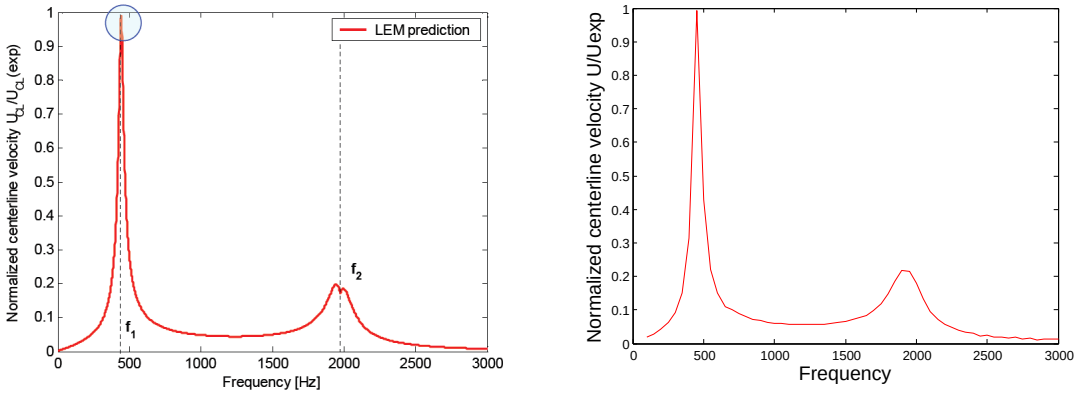

(a) LEM prediction (b) FDB prediction

Figure 3.3. Comparison LEM and FDB prediction for CFDVal2004 Workshop Case 1

Table 3.2. Properties of Piezoelectric-driven synthetic jet actuator used in CFDVal2004 Case 1 [6]

Brass Shim	Density (kg/m^3)	8700
	Thickness (mm)	0.15
	Diameter (mm)	49
Piezoceramic	Density (kg/m^3)	7700
	Thickness (mm)	0.31
	Diameter (mm)	24.4
Diaphragm	Compliance $(s^2.m^4/kg)$	5.80E-11
	Acoustic Mass (kg/m^4)	2.06E+03
	Acoustic piezoelectric coefficient da (m^3/V)	1.28E-10
	Natural frequency Hz	2114
Orifice	Diameter (mm)	1.27
	Helmholtz frequency (Hz)	977
Forcing	Voltage amplitude (V)	101.8
	Force amplitude (N)	0.9925

It can be seen from these figures that there is a good agreement between the present model and LEM.

3.3. STOCHASTIC PROBLEMS

3.3.1. Case 1. The stochastic model problem for Case 1 was formulated by introducing uncertainties in the amplitude F and frequency f of the input force $F(t)$.The parameters $F = F(\xi_1)$ and $f = f(\xi_2)$ are modeled as uniform uncertain

variables with a mean value of $F = 0.574N$ and $f = 2184Hz$. The uncertainty range chosen for force amplitude was [0.5453,0.6027] and that for frequency was [2074.8, 2293.2] corresponding to $\pm 5\%$ variation from the mean. Here ξ_1 and ξ_2 are standard uniform random variables defined in the interval [-1, 1], which have a constant PDF of 0.5. Due to the uniform nature of the input uncertainties, the Legendre polynomials were used as the basis functions in the polynomial chaos expansions. The convergence of the NIPC expansion was studied up to fifth order expansion. With an oversampling ratio of two and two input uncertain variables this required 42 evaluation in the sample space. Figure 3.4 shows the Latin Hypercube sample points at which the model was evaluated.

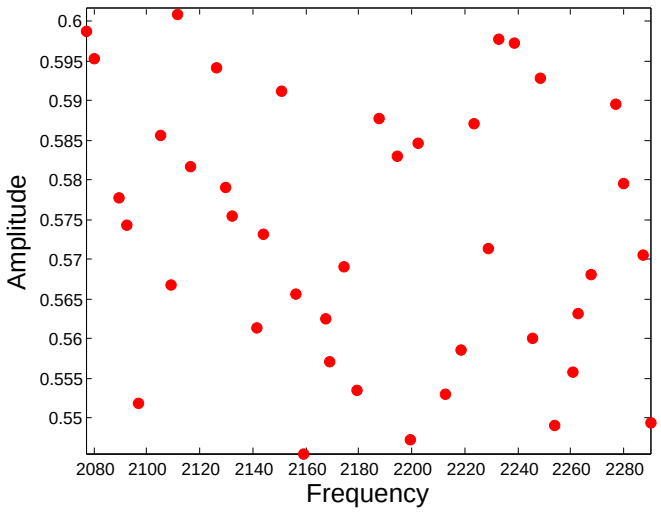

Figure 3.4. Model Problem Case 1 sample points

Figure 3.5(a) and 3.5(b) shows the convergence of the Mean and Standard deviation with increasing order of the polynomial expansion and Figure 3.6 shows the convergence of the CDFs. It is clear from these figures that the solution is converged at 5^{th} degree.

Table 3.3 compares the results from the NIPC method with direct Monte Carlo sampling of the model problem. The Mean and Standard Deviations compare very well between the two approaches.

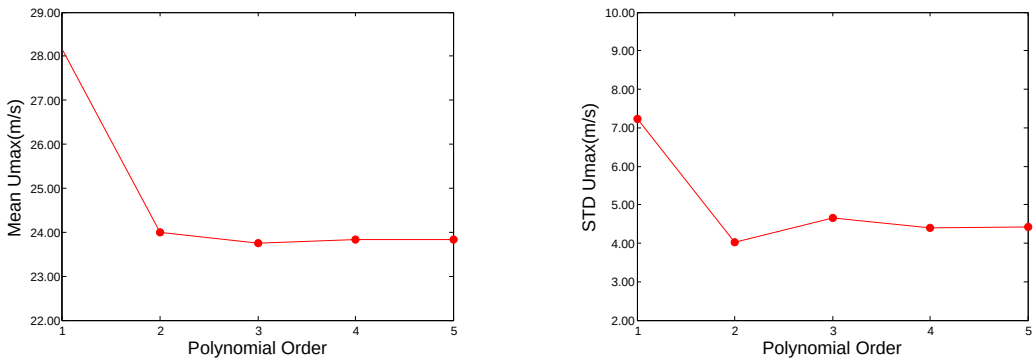

(a) Convergence of Mean (b) Convergence of STD

Figure 3.5. Convergence of Mean and STD with increasing polynomial order-Case1

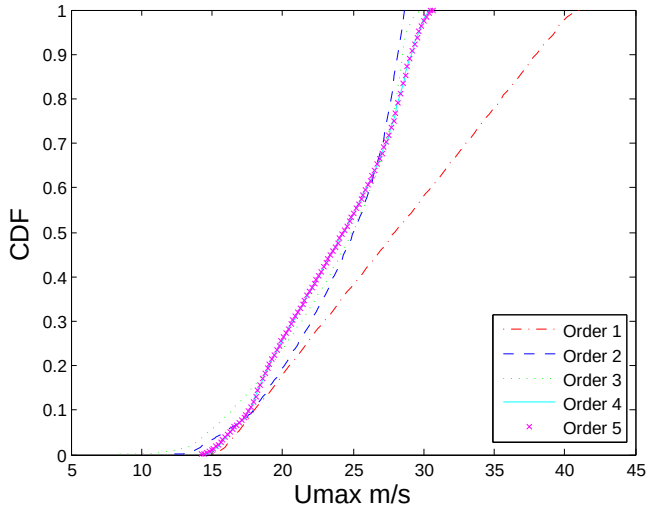

Figure 3.6. Convergence of CDF with increasing polynomial order Case 1

Note that 100,000 samples have been used in the Monte Carlo sampling. Hence it can be seen that the NIPC method offers an efficient way of estimating the uncertainty statistics requiring just 42 evaluations of the model. Figures 3.7(a)and 3.7(b) also show the comparison of the maximum output velocity distribution from the two models. As can be seen, the two distributions compare very well.

Table 3.3. Comparison of NIPC with MC for Case 1

	Mean	%Difference	STD	%Difference
NIPC	23.83691	0.06022362	4.421428	0.32954742
MC	23.82257		4.436047	

A Global sensitivity analysis was performed to measure the importance of individual uncertain random variables on the overall uncertainty in an output variable of interest. A total of 100,000 samples were created using the 5^{th} order stochastic response. Figures 3.8(a) and 3.8(b) show the scatter plot of exit plane U_{max} with respect to frequency and amplitude, respectively. Qualitatively, it can be seen from Figures 3.8(a) and 3.8(b) that U_{max} is highly sensitive to the frequency and not as much to the amplitude. The narrow band in 3.8(a) indicates that for a constant frequency the variation in the output due to the variation in amplitude is relatively less. On the other hand, the wide scatter in the Figure 3.8(b) indicates that for constant amplitude, the variation in frequency causes a relatively higher variation in the output.

3.3.2. Case 2. The stochastic problem in the CFDVal2004 test case was again formulated by introducing uncertainties in the amplitude F and frequency f of the input force $F(t)$. The parameters $F = F(\xi_1)$ and $f = f(\xi_2)$ are modeled as uniform uncertain random variables with a mean value of $F = 0.9925N$ and $f = 460.2Hz$. The uncertainty range chosen for the amplitude was [0.9428,1.0421] and that for frequency was [437.19, 483.21] corresponding to $\pm 5\%$ variation from the mean. Here again ξ_1 and ξ_2 are standard uniform random variables defined in the interval [-1, 1], which have a constant PDF of 0.5. Due to the uniform nature of the input uncertainties, the Legendre polynomials were used as the basis functions in the polynomial chaos expansions. The convergence of the NIPC expansion was studied up to fifth order expansion. With an oversampling ratio of two and two input uncertain variables this required 42 evaluation in the sample space. Figure 3.9 shows the sample points at which the model was evaluated.

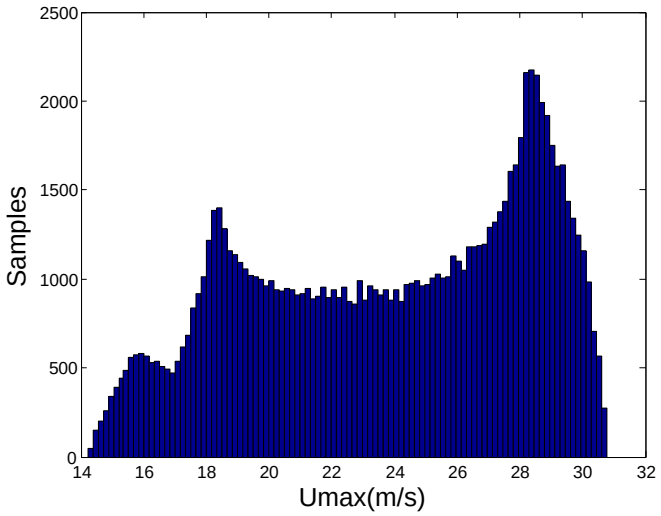

(a) Distribution of Umax from NIPC

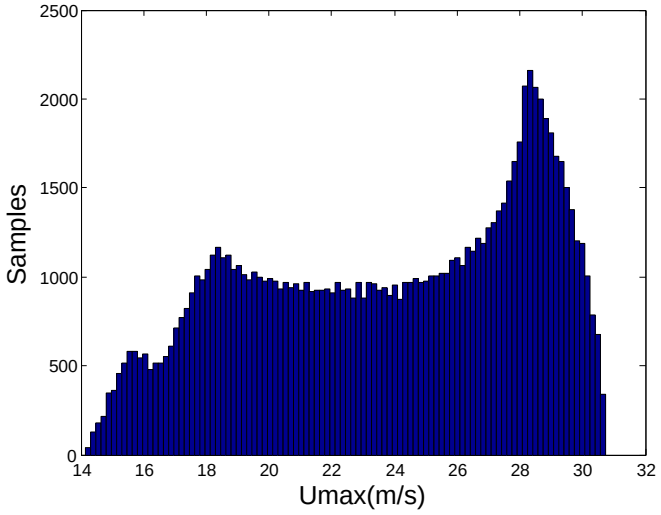

(b) Distribution of Umax from MC

Figure 3.7. Comparison of Umax distribution between NIPC and direct MC Case 1.

Figures 3.10(a) and 3.10(b) show the convergence of the Mean and Standard deviation and Figure 3.11 shows the convergence of the CDFs with increasing order of polynomial expansion. It is clear from these figures that the solution is converged at 5^{th} degree.

Table 3.4 compares the results from the NIPC method with direct Monte Carlo sampling of the model problem. As in Case 1, 100,000 points in the sample space were used to perform Monte Carlo.

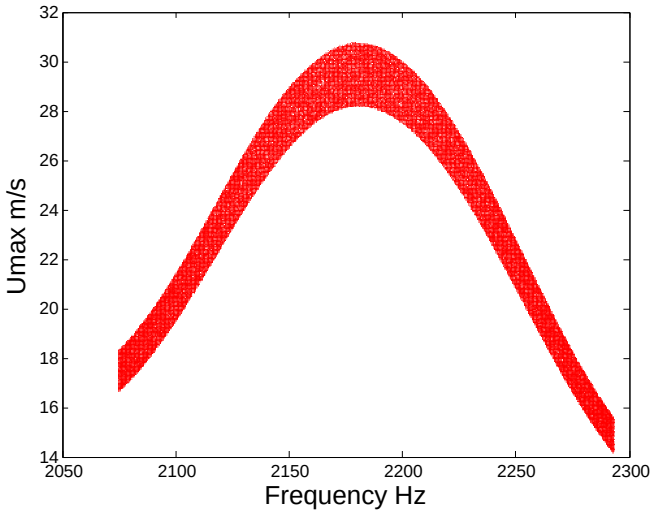

(a) Sensitivity to frequency

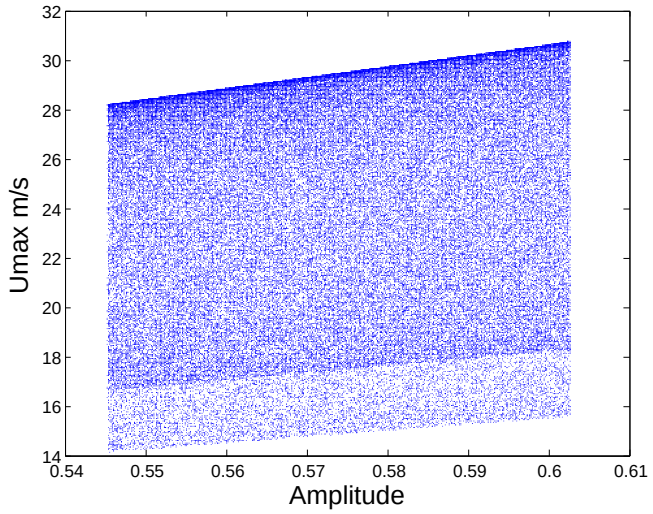

(b) Sensitivity to Amplitude

Figure 3.8. Sensitivity Analysis of U_{max} with respect to Frequency and Amplitude for stochastic model problem-Case 1.

The results compare very well indicating that the 5^{th} degree polynomial is sufficient to generate the same quality statistics as Monte Carlo. Figures 3.12(a)and 3.12(b) also show the comparison of the maximum output velocity distribution from the two models. The two distributions again compare well.

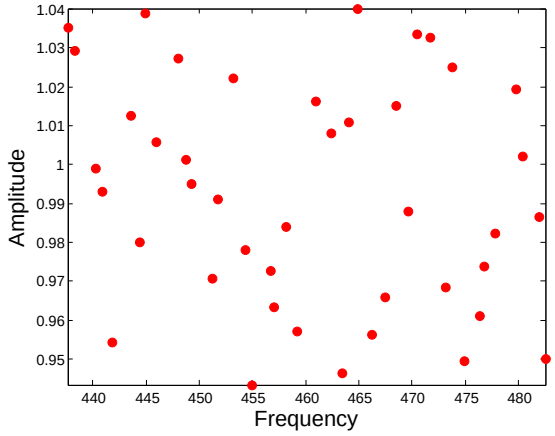

Figure 3.9. Model Problem Case 2 sample points

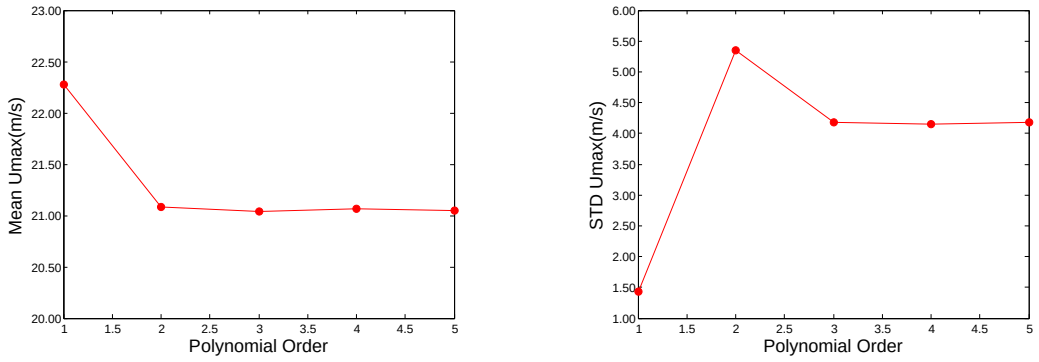

(a) Convergence of Mean

(b) Convergence of STD

Figure 3.10. Convergence of Mean and STD with increasing polynomial order-Case 2

A similar Global Sensitivity Analysis as described for Case 1 was performed for Case 2. Figures 3.13(a) and 3.13(b) show the scatter plot of exit plane U_{max} with respect to frequency and amplitude, respectively, for Case 2. As in Case 1, it can be seen from figure 3.13(a) and 3.13(b) that U_{max} is highly sensitive to the frequency and not as much to the amplitude. The narrow band in 3.13(a) indicates that for a constant frequency the variation in the output due to the variation in amplitude is relatively less. On the other hand, the wide scatter in 3.13(b) indicates that for constant amplitude, the variation in frequency causes a relatively higher variation in the output.

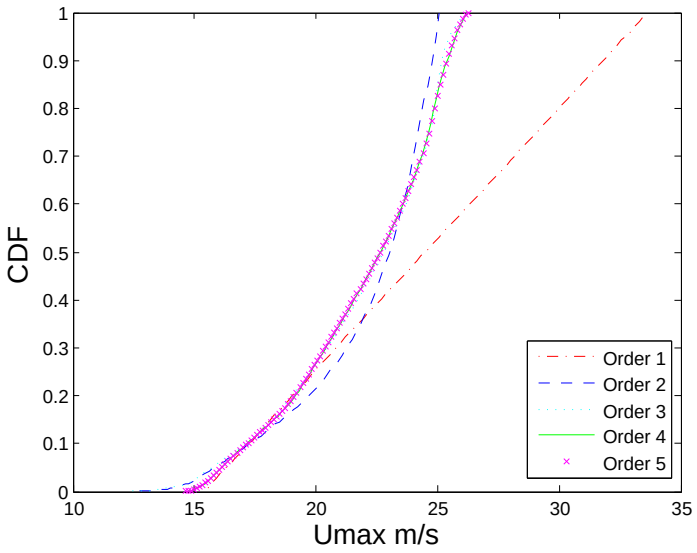

Figure 3.11. Convergence of CDF with increasing polynomial order Case 2

Table 3.4. Comparison of NIPC with MC for Case 2

	Mean	%Difference	STD	%Difference
NIPC	22.0297	0.0553	3.0458	0.2036
MC	22.0401		3.0395	

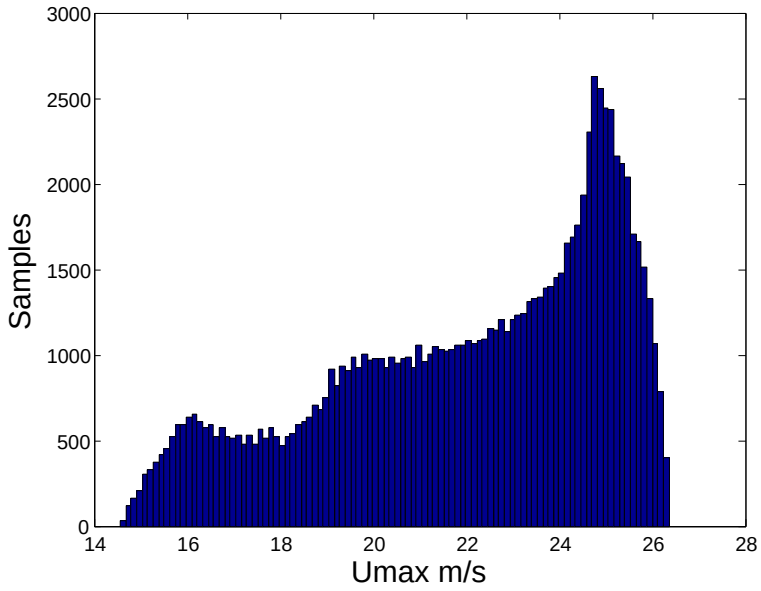

(a) Distribution of Umax from NIPC Case 2

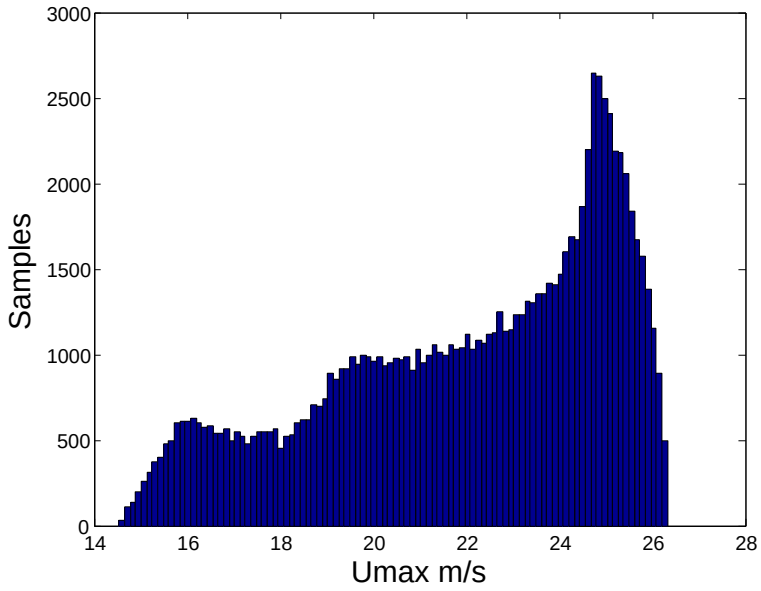

(b) Distribution of Umax from MC Case 2

Figure 3.12. Comparison of Umax distribution between NIPC and direct MC Case 2

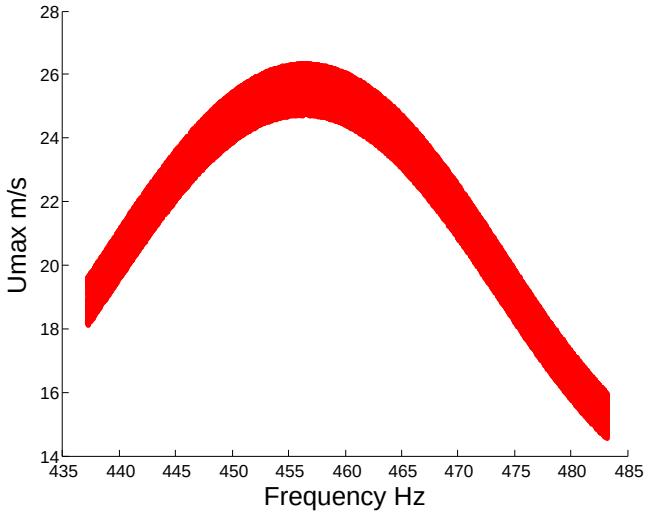

(a) Sensitivity to frequency

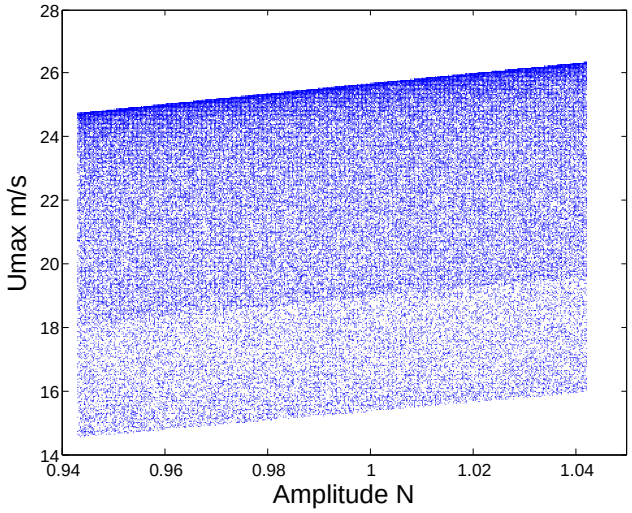

(b) Sensitivity to Amplitude

Figure 3.13. Sensitivity Analysis of U_{max} with respect to Frequency and Amplitude Case 2

4. UNCERTAINTY QUANTIFICATION IN CFD SIMULATIONS

This section introduces the basics of computational modeling and the governing equations used in formulating the synthetic jet actuator case. The $k-\omega$ model used for solving the turbulent RANS equations is also briefly discussed. Section 4.2 explains the geometry of the actuator used in the CFDVal2004 workshop test case followed by the description of the CFD case setup and the boundary conditions applied. The formulation of the stochastic CFD problem is described in Section 4.6 and the convergence study and results and discussion are presented in the subsequent sections.

4.1. INTRODUCTION TO CFD

Computational Fluid Dynamics (CFD) is the analysis of systems involving fluid flow, heat transfer and associated phenomena by means of computer-based simulation. The physical aspects of any fluid flow are governed by the three fundamental principles of conservation of mass,momentum and energy.These fundamental principles can be expressed in terms of mathematical equations, which are usually partial differential equations. In Anderson [27], computational fluid dynamics is defined as "the art of replacing the integrals or the partial derivatives (as the case may be) in these equations with discretized algebraic forms, which in turn are solved to obtain numbers for the flow field values at discrete points in time and/or space."

4.1.1. Governing Equations. Since the evolution of the vortical structures from the Synthetic Jet Actuator is turbulent in nature, it becomes computationally very expensive to directly solve the governing equations. In the current study Reynolds-Averaged Navier-Stokes were solved to model the transport of the averaged flow quantities. In this technique the instantaneous flow variables in the Navier-Stokes equation is decomposed into mean and fluctuating components. For example the

velocity in the flow field is decomposed as

$$u_i = \bar{u_i} + u_i' \tag{19}$$

where $\bar{u}_i$ and u_i' are the mean and fluctuating velocity components ($i = 1, 2, 3$). Similarly, for pressure and other scalar quantities:

$$\phi = \bar{\phi} + \phi' \tag{20}$$

where ϕ denotes a scalar such as pressure, energy, or species concentration. Thus by substituting instantaneous flow quantities with expressions of the form Equations 19 and 20 in the exact Navier-Stokes equation and taking a time average of it will result in the Reynolds-Averaged Navier-Stokes equations which can be represented as below:

$$\frac{\partial \rho}{\partial t} + \frac{\partial}{\partial x_i}(\rho u_i) = 0 \tag{21}$$

$$\frac{\partial}{\partial t}(\rho u_i) + \frac{\partial(\rho u_i u_j)}{\partial x_j} = -\frac{\partial p}{\partial x_i} + \frac{\partial}{\partial x_i}\left[\mu(\frac{\partial u_i}{\partial x_j} + \frac{\partial u_j}{\partial x_i} - \frac{2}{3}\delta_{ij}\frac{\partial u_l}{\partial x_l}\right] + \frac{\partial}{\partial x_j}(-\rho\overline{u_i' u_j'}) \tag{22}$$

Please note that the over-bar on the mean component has been dropped to keep the equation simple. Also the energy equation was not solved hence it is not included here. The Reynolds stresses, $-\rho\overline{u_i' u_j'}$, must be modeled in order to close these equations. A common method to estimate this quantity is by applying the Boussinesq Hypothetis which relates the Reynolds stresses to the mean velocity gradients as follows:

$$-\rho\overline{u_i' u_j'} = \mu_t \left(\frac{\partial u_i}{\partial x_j} + \frac{\partial u_j}{\partial x_i}\right) - \frac{2}{3}\left(\rho k + \mu_t \frac{\partial u_k}{\partial x_k}\right)\delta_{ij} \tag{23}$$

4.1.2. k-ω Turbulence Model. The Boussinesq hypothesis is used in the Spalart-Allmaras model, the k- ϵ models, and the k- ω models. The current study utilizes the Menter Shear-Stress-Transport k- ω model [28] to solve the RANS equations. Along with the RANS equations, the SST k- ω model solves the following two additional

equations for k and ω so that μ_t can be computed as a function of k and ω [29]:

$$\frac{\partial}{\partial t}(\rho k) + \frac{\partial}{\partial x_i}(\rho k u_i) = \frac{\partial}{\partial x_j}\left(\Gamma_k \frac{\partial k}{\partial x_j}\right) + \tilde{G}_k - Y_k + S_k \tag{24}$$

$$\frac{\partial}{\partial t}(\rho \omega) + \frac{\partial}{\partial x_i}(\rho \omega u_i) = \frac{\partial}{\partial x_j}\left(\Gamma_\omega \frac{\partial \omega}{\partial x_j}\right) + G_\omega - Y_\omega + D_\omega + S_\omega \tag{25}$$

where the effective diffusivity is given by

$$\Gamma_k = \mu + \frac{\mu_t}{\sigma_k} \tag{26}$$

$$\Gamma_\omega = \mu + \frac{\mu_t}{\sigma_\omega} \tag{27}$$

The turbulent viscosity is computed as follows:

$$\mu_t = \frac{\rho k}{\omega} \frac{1}{\max\left[\frac{1}{\alpha^*}, \frac{SF_2}{a_1 \omega}\right]} \tag{28}$$

$$\sigma_k = \frac{1}{F_1/\sigma_{k,1} + (1 - F_1)/\sigma_{k,2}} \tag{29}$$

$$\sigma_\omega = \frac{1}{F_1/\sigma_{\omega,1} + (1 - F_1)/\sigma_{\omega,2}} \tag{30}$$

The coefficient α^* that damps the turbulent viscosity causing a low-Reynolds-number correction is given by

$$\alpha^* = \alpha^*_\infty \left(\frac{\alpha^*_0 + \mathrm{Re}_t/R_k}{1 + \mathrm{Re}_t/R_k}\right) \tag{31}$$

The blending functions F_1 and F_2 are given by

$$F_1 = \tanh\left(\Phi_1^4\right) \tag{32}$$

$$\Phi_1 = \min\left[\max\left(\frac{\sqrt{k}}{0.09\omega y}, \frac{500\mu}{\rho y^2 \omega}\right), \frac{4\rho k}{\sigma_{\omega,2} D^+_\omega y^2}\right] \tag{33}$$

$$D_{\omega}^{+} = \max\left[2\rho\frac{1}{\sigma_{\omega,2}}\frac{1}{\omega}\frac{\partial k}{\partial x_j}\frac{\partial \omega}{\partial x_j}, 10^{-10}\right] \tag{34}$$

$$F_2 = \tanh\left(\Phi_2^2\right) \tag{35}$$

$$\Phi_2 = \max\left[2\frac{\sqrt{k}}{0.09\omega y}, \frac{500\mu}{\rho y^2 \omega}\right] \tag{36}$$

The term $\tilde{G}_k$ represents the production of turbulence kinetic energy, and is defined as:

$$\tilde{G}_k = \min(G_k, 10\rho\beta^* k\omega) \tag{37}$$

where the turbulent kinetic energy production term is given by

$$G_k = \mu_t S^2 \tag{38}$$

and S, the strain rate tensor is given by

$$S \equiv \sqrt{2S_{ij}S_{ij}} \tag{39}$$

The mean strain rate tensor is defined as

$$S_{ij} = \frac{1}{2}\left(\frac{\partial u_j}{\partial x_i} + \frac{\partial u_i}{\partial x_j}\right) \tag{40}$$

The term G_ω represents the production of ω and is given by

$$G_\omega = \frac{\alpha}{\nu_t} G_k \tag{41}$$

The term Y_k representing the dissipation of the turbulent kinetic energy is given by

$$Y_k = \rho\beta^* k\omega \tag{42}$$

The term Y_ω represents the dissipation of ω and is given by

$$Y_\omega = \rho\beta\omega^2 \tag{43}$$

The SST model is based on both $k-\omega$ and $k-\epsilon$ models. Hence in order to blend the two models a cross-diffusion modification term is defined that is given by

$$D_\omega = 2\left(1-F_1\right)\rho\sigma_{\omega,2}\frac{1}{\omega}\frac{\partial k}{\partial x_j}\frac{\partial \omega}{\partial x_j} \tag{44}$$

The remaining model constants are listed below

$$\sigma_{k,1} = 1.176, \quad \sigma_{\omega,1} = 2.0, \quad \sigma_{k,2} = 1.0, \quad \sigma_{\omega,2} = 1.168$$

$$a_1 = 0.31, \quad \beta_{i,1} = 0.075 \quad \beta_{i,2} = 0.0828$$

$$\alpha^*_\infty = 1, \quad \alpha_\infty = 0.52, \quad \alpha_0 = \tfrac{1}{9}, \quad \beta^*_\infty = 0.09, \quad \beta_i = 0.072, \quad R_\beta = 8$$

$$R_k = 6, \quad R_\omega = 2.95, \quad \zeta^* = 1.5, \quad \mathrm{M}_{t0} = 0.25, \quad \sigma_k = 2.0, \quad \sigma_\omega = 2.0$$

4.2. GEOMETRY

This case uses the geometry used in Case1 of CFDVal2004 [30] and models a synthetic jet issuing into quiescent air out of a rectangular slot 0.05" wide and 1.4" long. The actuator is flush mounted on an aluminum plate, 0.25" thick, enclosed by a 2'x2'x2' glass enclosure. The enclosure helps to isolate the jet from the ambient air and also contains the seeding particles for the flow measurement. The slot is located at the center of the plate. Jet is produced by a circular piezo-electric diaphragm, 2" in diameter mounted on one side of the cavity beneath the plate. An O-ring seal clamps the diaphragm to the cavity, reducing the effective diameter available for oscillation, to 1.85". The diaphragm displacement is offset such that the displacement is less inwards and more outwards.

4.3. COMPUTATIONAL MODELING

The commercial CFD software, Fluent 6.3 [29], was used for the simulations. The unsteady Reynolds-Averaged Navier-Stokes (RANS) equations coupled with two-equation eddy viscosity SST k-omega turbulence model [28] were solved to compute the unsteady, turbulent, two dimensional flow both in the cavity and the main flow domain of quiescent air. The CFD validation workshop results indicated that a

two-dimensional flow assumption gave reasonable solutions in the near-field up to a location of 8 mm measured from the slot exit. Therefore in this study we also focused on the quantification of uncertainty in the near-field flow properties with a two-dimensional approach. A pressure-based solver was used in the computations with SIMPLE algorithm for velocity-pressure coupling. The inviscid fluxes were approximated with a second order upwind scheme in space and the viscous terms were approximated with second-order central differencing. A secondorder accurate implicit time-integration was used to advance the solution in time.

4.4. BOUNDARY CONDITIONS

Outflow boundary condition was imposed on the left, right and top boundaries of the domain (Figure 4.1(a)). The aluminum plate and the wall of the cavity were treated as non-slip wall boundaries. From the experiments, the diaphragm oscillation was available in terms of a time-dependent displacement profile measured at the center of the diaphragm [30]. For computations, a cosine curve was fit to this data and the velocity was obtained by taking a time derivative of the resulting displacement profile.In Equation 45, D represents the displacement of the center of the piezo-electric membrane, a_0 represents the amplitude of displacement (0.2863 mm) and C is a constant to account for the offset in the displacement (-0.125 mm). In Equation 46, A_0 is the amplitude and f is the frequency of the membrane velocity. This unsteady velocity information was then used as a time-dependent inlet velocity boundary condition in the CFD simulations. It should be noted that, the current study modeled the membrane as a piston with a uniform velocity imposed on the entire face given by Equation 46.

$$D = a_0 cos(2\pi f t) + C \tag{45}$$

$$U = A_0 sin(2\pi f t) \tag{46}$$

4.5. GRID AND TEMPORAL RESOLUTION

In order to accurately reproduce the experimental and CFD results from the workshop, this study used the grid made available on the CFDVAL2004 website [30]. The grid is made up of nine zones. Two levels of grid densities (coarse and fine) were available from the workshop. The current study utilized the fine mesh with a total number of 198,545 grid points (Figure 4.1(a)). As for the time step size, each cycle of the membrane oscillation was divided into 1000 time steps with each time step corresponding to 2.248710^{-6} seconds. To achieve convergence at every time step, 15 inner iterations were performed. Figure 4.2 shows the u-velocity contour plot at 90 deg phase angle with the baseline configuration which gives a snapshot of the counter rotating vortex pairs, generated by the membrane oscillation, rising into the quiescent air domain. The periodicity in the output quantities were achieved after two complete cycles. The average was taken over the next cycle to obtain all the long-time averaged quantities.The Baseline results and the results from the CFDVal2004 workshop have been included in APPENDIX B. The results agreed well with the experimental measurements at most of the locations and the trends were similar to the results submitted at the workshop. A step-by-step procedure of the CFD case setup in FLUENT is explained in APPENDIX C.

4.6. DESCRIPTION OF THE STOCHASTIC PROBLEM

The stochastic problem was formulated by introducing uncertainties in the amplitude (A_0) and frequency (f) of the unsteady velocity inlet boundary condition used to model the oscillation of the piezo-electric membrane in the cavity (Equation 46). The parameters $A_0 = A_0(\xi_1)$ and $f = f(\xi_2)$ were modeled as uniform uncertain variables with the mean values of 0.8 (m/s) for the amplitude and 444.7 Hz for the frequency. The uncertainty range was chosen to be [0.76, 0.84] (m/s) for the amplitude and [422.465, 466.935] (Hz) for the frequency.

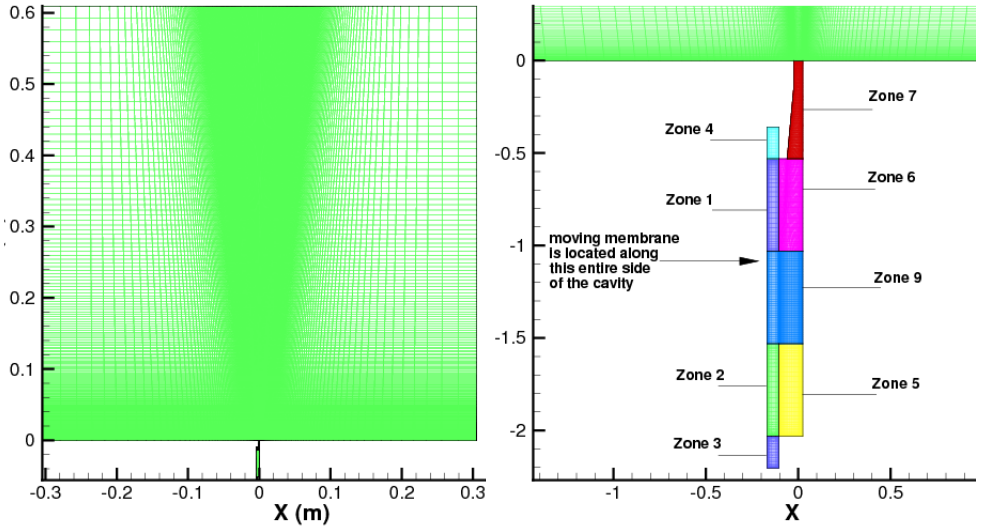

(a) Full Domain (b) Descretized Cavity

Figure 4.1. Descretized Domain

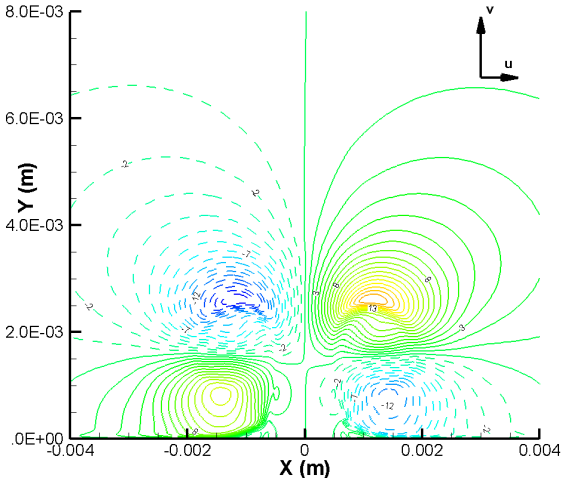

Figure 4.2. Instantaneous u-velocity contour plot above the slot exit at 90 deg phase angle (baseline case) after the periodicity in u-velocity is achieved.

This corresponds to a $\pm 5\%$ change from the corresponding mean values to demonstrate the application of the NIPC method for uncertainty quantification. The same procedure can be followed when specific uncertainty information from experiments becomes available. Here (ξ_1) and (ξ_2) are standard uniform random variables de-

fined in the interval [-1, 1], which have a constant PDF of 0.5. Due to the uniform nature of the input uncertainties, the Legendre polynomials were used as the basis functions in the polynomial chaos expansions. For the construction of the stochastic response surface with Point Collocation NIPC, 42 collocation points were selected in random space by Latin HyperCube sampling (Figure 4.3), which corresponds to an oversampling ratio of 2 for a 5^{th} degree polynomial of two random variables.

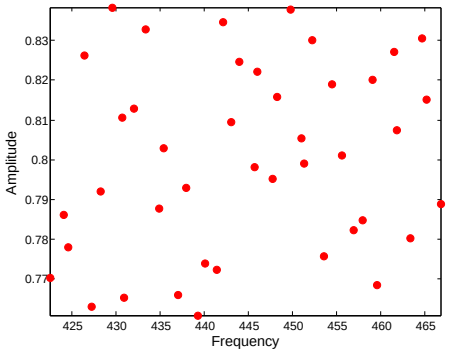

Figure 4.3. LHS Samples for 2 input variables CFD case

For uncertainty quantification, long-time averaged u and v velocity components at three different stations were considered ($y = 0.1mm, y = 1mm$ and $y = 4mm$ above the slot exit) . To obtain the statistics, polynomial chaos expansions at each point were evaluated with 10,000 uniform random samples $(\xi_1, \xi_2)_i, i = 1, , 10000)$.Note that there is no relation between the number of samples used to evaluate the statistics and the deterministic CFD simulations, which were used to obtain the coefficients of the polynomial chaos expansion given by Equation 1. Once the expansion is available one can perform a separate, large number of sampling to calculate the uncertainty statistics since evaluating the polynomial chaos expansion will be computationally inexpensive.

4.7. CONVERGENCE STUDIES

Figure 4.4(a) through 4.4(d) shows the convergence of Mean and Standard deviation at the location $x = 0, y = 4mm$ for both long-time averaged u and v-velocities.

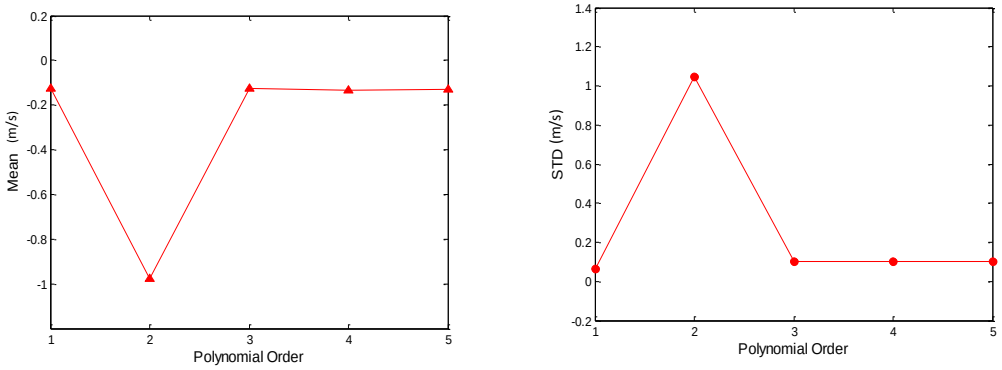

(a) Convergence Mean of u-velocity

(b) Convergence STD of u-velocity

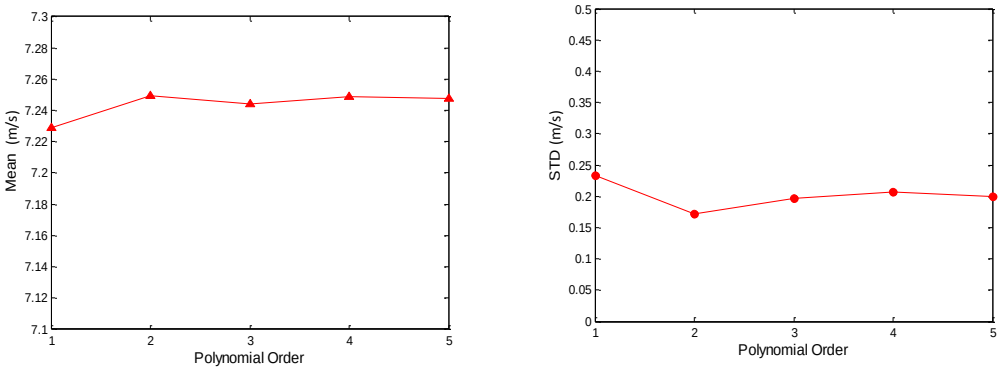

(c) Convergence Mean of v-velocity

(d) Convergence STD of v-velocity

Figure 4.4. Convergence of Mean and STD of u and v-velocity at $(x = 0, y = 4mm)$

It can be seen from these plots that the both the mean and standard deviation are completely converged to the 5^{th} degree polynomial. The percentage error in Mean between the 4^{th} and the 5^{th} degree polynomial for v-velocity at this location was found to be 0.01% and that for STD was found to be 3.42%. The percentage error in Mean between the 4^{th} and the 5^{th} degree polynomial for u-velocity at the same location was found to be 2.05% and that for STD was found to be 0.38%. Similar trends can be seen at all the other locations.

Figure 4.5(a) through 4.5(d) show the convergence of CDFs of the long-time averaged v and u-velocities for different polynomial orders. It can be seen from these figures that the CDFs for the forth and fifth order polynomials lie almost exactly on top of each other. The convergence of the 95% confidence intervals for long-time averaged v and u velocities at $y = 0.1mm$ and $y = 4mm$ lines are given in Figure 4.6(a) through 4.7(a). Again the confidence interval bars overlap each other as the polynomial order increases. Based on these convergence studies, fifth order polynomial chaos expansion was used to generate all the uncertainty statistics.

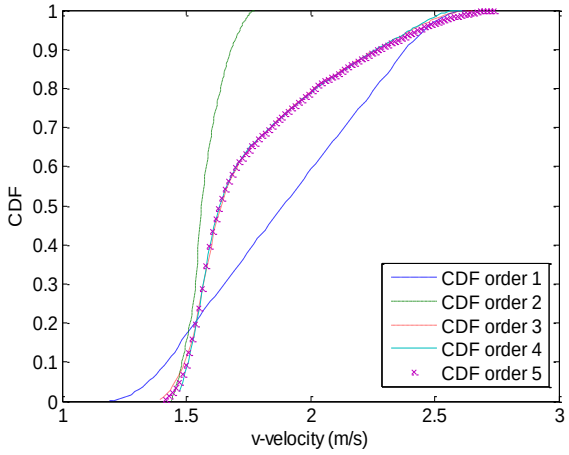

(a) CDF of v-velocity at $(x = 0, y = 0.1mm)$

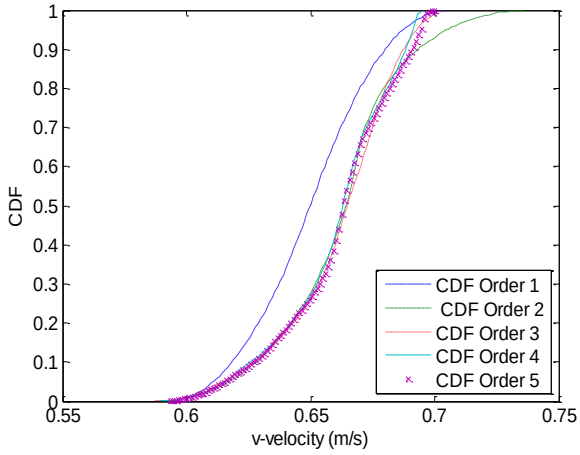

(b) CDF of u-velocity at $(x = 0, y = 0.1mm)$

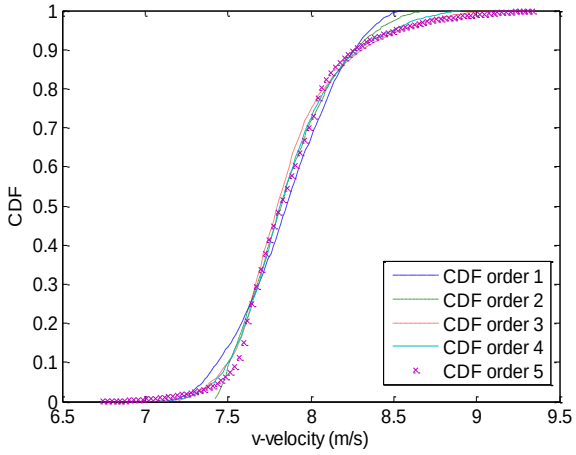

(c) CDF of v-velocity at $(x = 0, y = 4mm)$

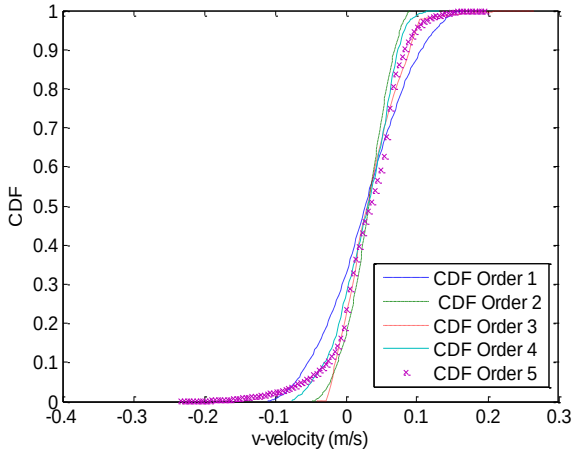

(d) CDF of u-velocity at $(x = 0, y = 4mm)$

Figure 4.5. Comparison of CDFs for different polynomial orders at $x = 0, y = 0.1mm$ and at $x = 0, y = 4mm$

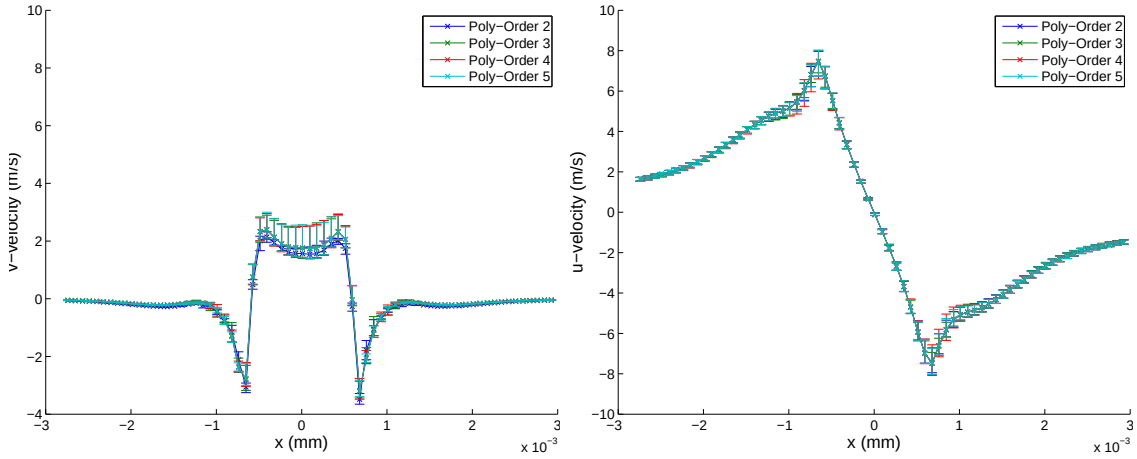

(a) CI convergence of v-velocity (b) CI convergence of u-velocity

Figure 4.6. Comparison of CIs for different polynomial orders at $x = 0, y = 0.1mm$

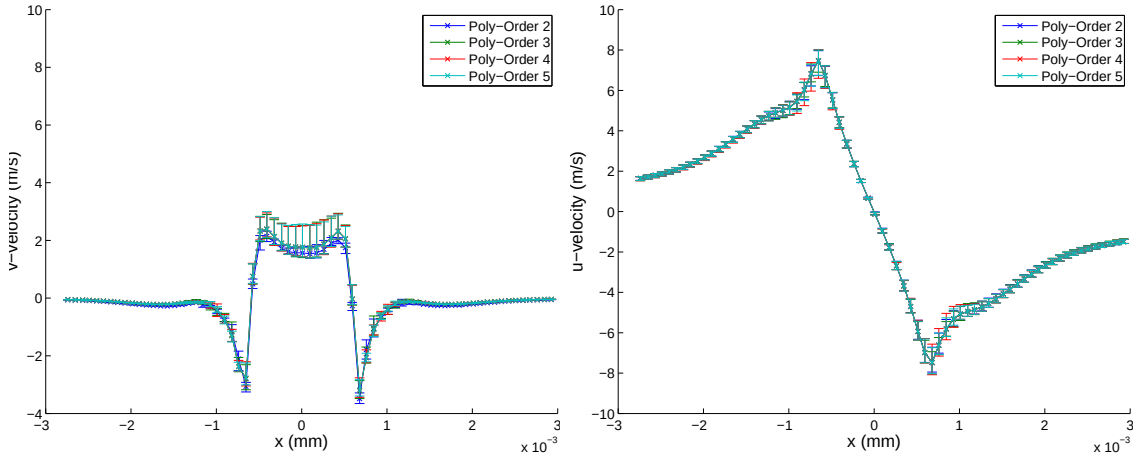

(a) CI convergence of v-velocity (b) CI convergence of u-velocity

Figure 4.7. Comparison of CIs for different polynomial orders at $x = 0, y = 4mm$

4.8. UNCERTAINTY QUANTIFICATION RESULTS AND DISCUSSION

Figures 4.8(a) through 4.10(b) show the mean and 95% CIs for the long-time averaged u and v velocities at three y stations ($y = 0.1mm, y = 1.0mm$, and $y = 4.0mm$) obtained with the 5^{th} order polynomial chaos expansions at each point. It can be seen from Figures 4.8(a), 4.9(a) and 4.10(a) that the uncertainty in the v velocity profile is higher directly above the slot exit compared to the regions to the left and right of the slot for all y stations studied. On the other hand, the uncertainty in the u velocity (Figures 4.8(b), 4.9(b) and 4.10(b)) is minimum at the centerline (x=0.0 mm), which is consistent with the motion of the vortices above the slot. The u-velocity profiles at these locations are least uncertain due to the fact that the vortex pairs are symmetric about the center of the slot. The uncertainty in u-velocity is higher just adjacent to the slot on either sides. It can be seen from Figure 4.10(b) that there is a large variation induced in the region adjacent to the slot at $y = 4mm$, above the slot exit, as a result of the uncertainty in the input amplitude and frequency. The experimental results obtained from the PIV measurements are also included for reference. For the v velocity distribution at $y = 0.1mm$, even with a relatively large uncertainty introduced to the amplitude and the frequency of the membrane motion, the discrepancy between experiment and the simulations above the slot exit cannot be captured. The same observation can be made for the u velocity especially away from the slot exit at $y = 0.1mm$ location. Similar trends were seen in all the other results from the CFDVal2004 workshop. This may indicate that the discrepancy at this location may be due to the other uncertainty sources in CFD (e.g., turbulence modeling or the boundary conditions) and/or the uncertainties in the measurements.

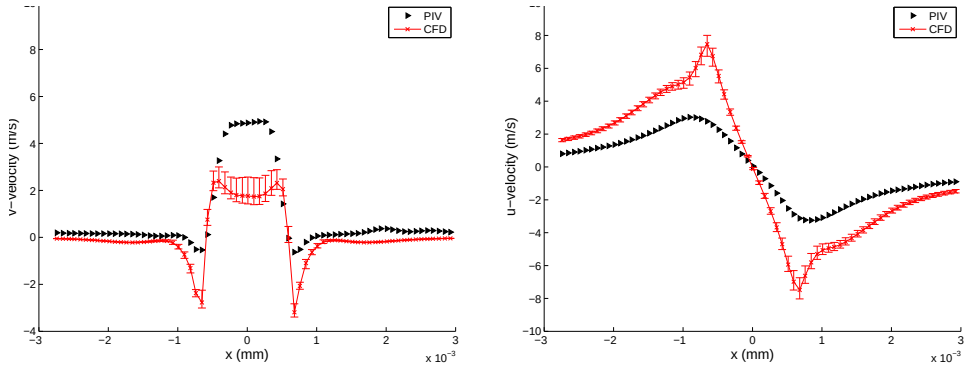

(a) CI of v-velocity at 0.1mm (b) CI of u-velocity at 0.1mm

Figure 4.8. 95% Confidence Interval of u and v-velocity on $y = 0.1mm$ line

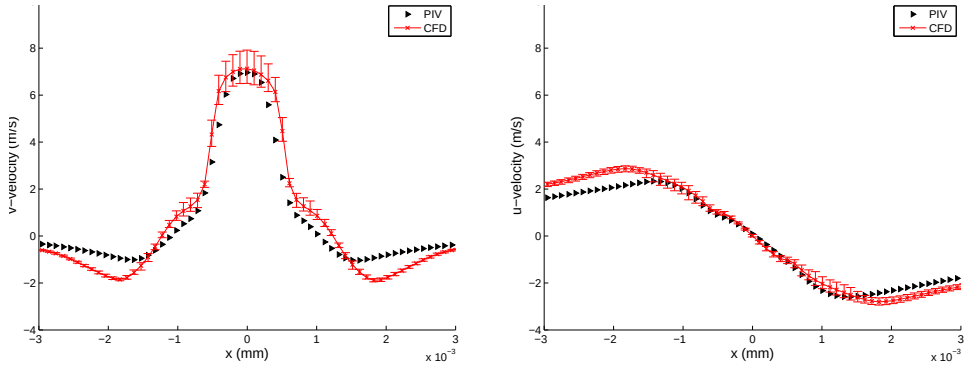

(a) CI of v-velocity at 1mm (b) CI of u-velocity at 1mm

Figure 4.9. 95% Confidence Interval of u and v-velocity on $y = 1mm$ line

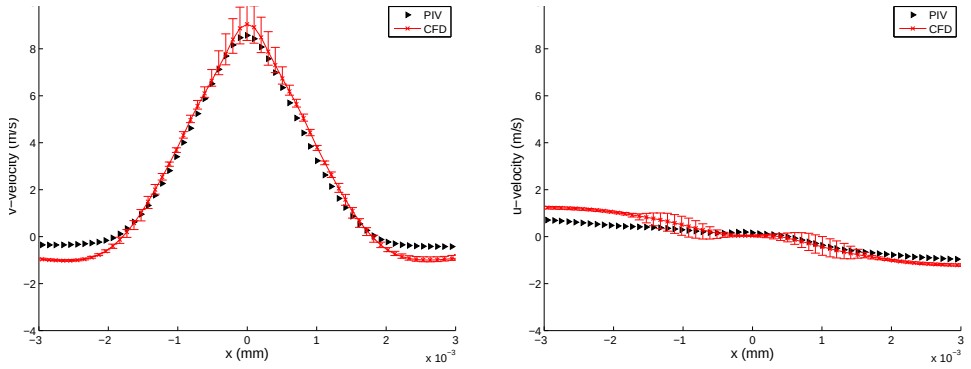

(a) CI of v-velocity at 4mm (b) CI of u-velocity at 4mm

Figure 4.10. 95% Confidence Interval of u and v-velocity on $y = 4mm$ line

Figures 4.11(a) through 4.13(b) show the standard deviation distribution at three different locations. As expected, the standard deviation is higher at the center of the slot for the v-velocities indicating that the variation of the long time averaged v-velocity profiles from the mean, in the region spanning the jet width, is much more compared to the regions to the left and right of the slot. Notice that the two lesser peaks on either sides of the slot width, in Figure 4.12(a), are at locations where the length of the 95% CI bars momentarily increases and then gradually fades out (Figure 4.9(a)). A similar trend can be seen in Figure 4.13(a). Also, it can be seen from plots 4.11(b), 4.12(b) and 4.13(b) that the peaks of the standard deviation curves for the u-velocity are on either sides of the slot width and the standard deviation is minimum at the center of the slot. This is also an acceptable trend since we have seen from the 95% CI plots (Figure 4.8(b), 4.9(b) and 4.10(b)) that the variation in u-velocity is more on either sides of the slot width regions and is very less at the center of the slot.

Figures 4.14 through 4.16 show the histograms for long-time averaged v-velocity at three different heights directly above the slot exit. It can be seen that the dependency of the v-velocity on the input stochastic variables (amplitude and the frequency of the piezo-electric membrane) is highly non-linear since the shapes of the histograms are quite different than a typical uniform distribution of both input variables.

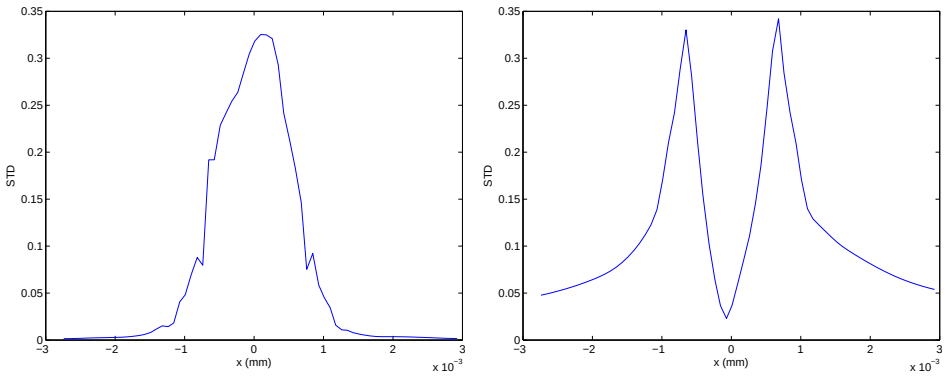

(a) STD of v-velocity (b) STD of u-velocity

Figure 4.11. STD of u and v-velocity on $y = 0.1mm$ line

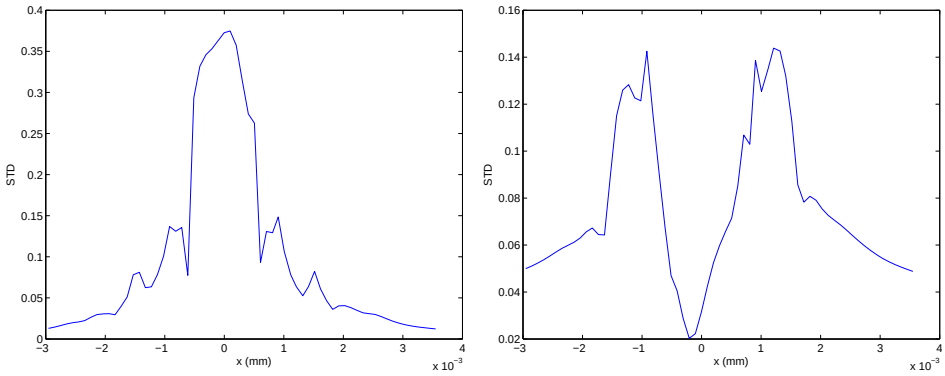

(a) STD of v-velocity (b) STD of u-velocity

Figure 4.12. STD of u and v-velocity on $y = 1mm$ line

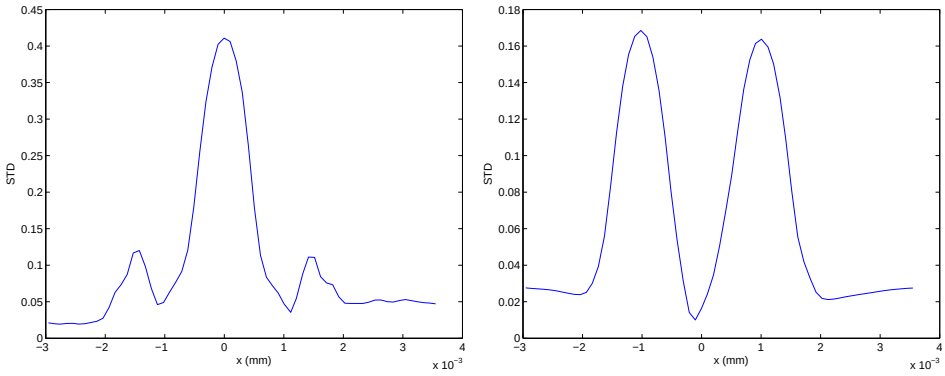

(a) STD of v-velocity (b) STD of u-velocity

Figure 4.13. STD of u and v-velocity on $y = 4mm$ line

The scatter plots of the various uncertain output parameters can be easily obtained by evaluating the corresponding polynomial chaos expansions ($P(\vec{\xi})$) with a large sample of scaled input uncertain variables ($\vec{\xi}$). Figures 4.17 to 4.20 show the scatter plot of longtime averaged v-velocity with respect to frequency and amplitude, respectively, at $(x = 0, y = 0.1mm)$.

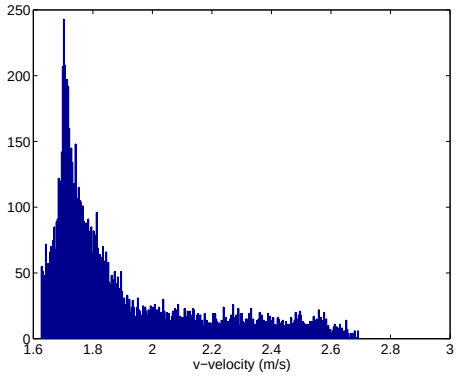

Figure 4.14. Histograms of long-time averaged v-velocity at (x=0,y=0.1mm)

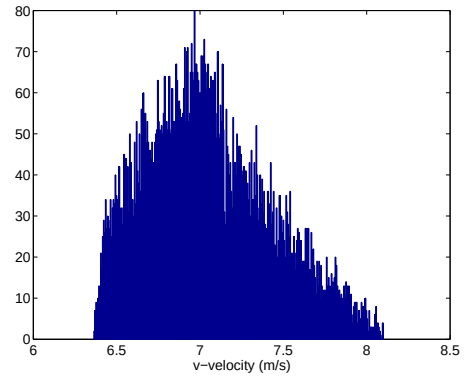

Figure 4.15. Histograms of long-time averaged v-velocity at (x=0,y=1mm)

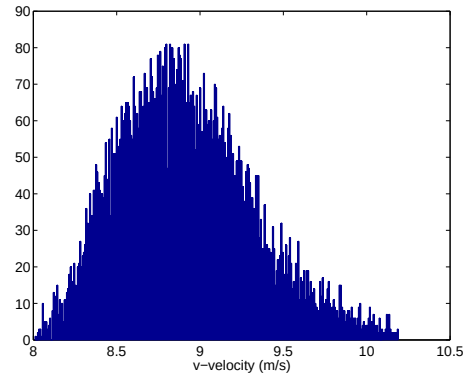

Figure 4.16. Histograms of long-time averaged v-velocity at (x=0,y=4mm)

With the help of these plots a Global Sensitivity Analysis can be performed using linear regression method to determine the sensitivity of the long-time averaged v-velocity (output parameter) to the variation in the input. It can be seen from Figure 4.17 and 4.18, that the long-time averaged v-velocity at this location is highly sensitive to frequency and not as much to the amplitude. The narrow band in Figure 4.17 indicates that for a constant frequency the variation in the output due to the variation in amplitude is relatively less. On the other hand, the wide scatter in Figure 4.18 indicates that for constant amplitude, the variation in frequency causes a relatively higher variation in the output. This fact is reinforced by comparing the correlation coefficients between the output and the two input parameters. In Figure 4.17 the correlation coefficient between v-velocity and frequency was found to be -0.7856 where as in Figure 4.18 the correlation coefficient between v-velocity and amplitude was found to be 0.1319. Correlation coefficient between long-time averaged v-velocity and frequency is higher in magnitude compared to that of amplitude indicating a higher sensitivity of the output to frequency at this location.

Figures 4.19 and 4.20 show the scatter plots of the long-time averaged v-velocity with frequency and amplitude respectively, at $x = 0, y = 4mm$ location. Here, it can be seen that both distributions are comparable. The correlation coefficient in figure 4.19 was found to be -0.7053 and that in figure 4.20 was found to be 0.7167. Hence it can be concluded that at this location both the input parameters have almost equal influence on the output.

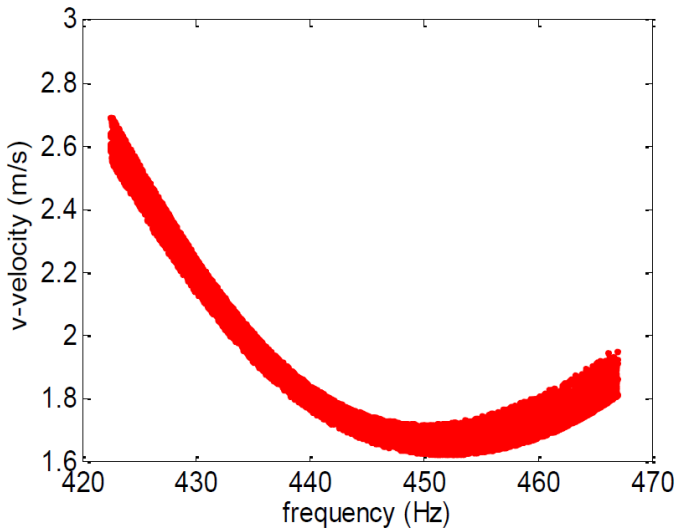

Figure 4.17. Sensitivity of long-time averaged v-velocity to frequency at (x=0,y=0.1mm)

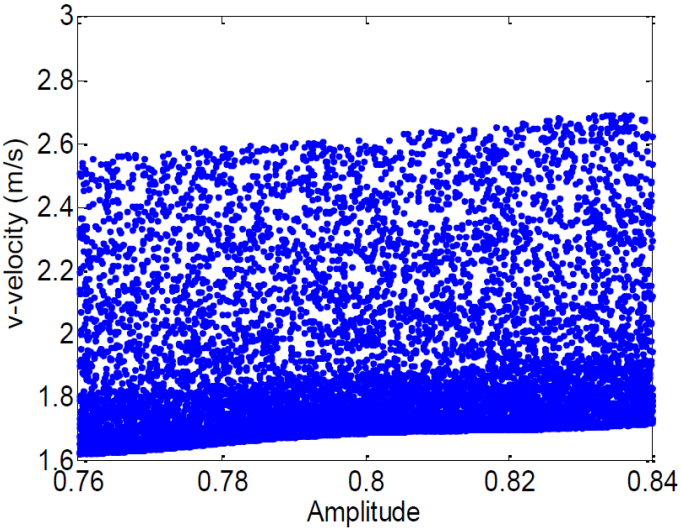

Figure 4.18. Sensitivity of long-time averaged v-velocity to Amplitude at (x=0,y=0.1mm)

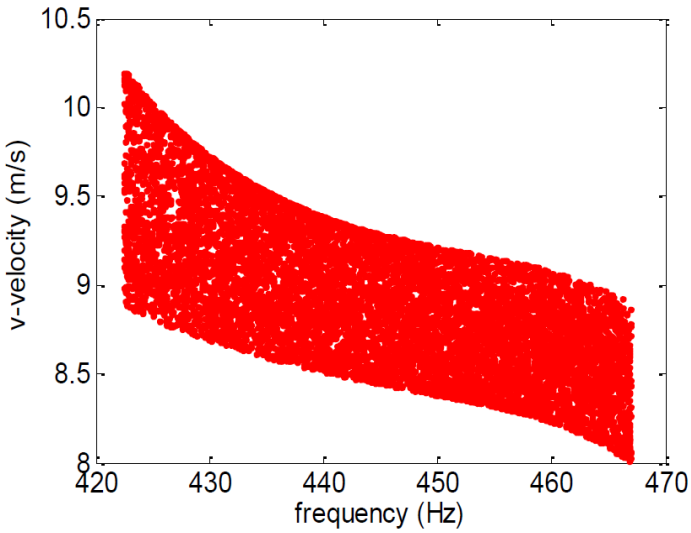

Figure 4.19. Sensitivity of long-time averaged v-velocity to frequency at (x=0,y=4mm)

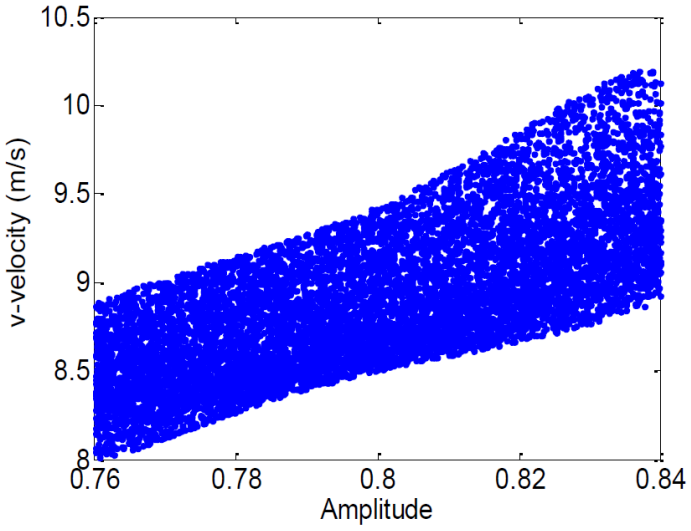

Figure 4.20. Sensitivity of long-time averaged v-velocity to Amplitude at (x=0,y=4mm)

5. CONCLUSIONS AND FUTURE WORK

5.1. CONCLUSIONS

The Point Collocation Non-Intrusive Polynomial Chaos method has been applied to two stochastic model problems and the CFD analysis of a synthetic jet problem that was used as a test case in the CFDVAL2004 workshop. The model problems were used to validate the Point-Collocation NIPC method with direct Monte Carlo sampling method. In both the model problem cases the NIPC results matched very well with that from Monte Carlo indicating the efficiency of the NIPC method in predicting the uncertainty statistics with very few number of sample evaluations.

The uncertainty quantification technique was applied to the CFD modeling of the synthetic jet actuator case to demonstrate the integration of computationally efficient uncertainty quantification to the high-fidelity CFD modeling of synthetic jet actuators. In this case, a synthetic jet issued into quiescent air and the long-time averaged u and v-velocity profiles were monitored at several locations above the slot exit. The amplitude and frequency of oscillation of the membrane in the cavity generating the synthetic jet were expected to have significant influence on the velocity profiles in the flow field. Therefore, the estimation of the uncertainty in long-time averaged velocity components, caused by the variation in these two parameters within the specified limits, was performed. Both uncertain variables (amplitude and frequency of the velocity of the membrane) were treated as uniform random variables. A fifth degree NIPC expansion obtained with Latin Hypercube sampling was found to be capable of estimating the statistics after a detailed convergence analysis. 42 deterministic CFD simulations were carried out with an oversampling ratio of two for the fifth degree polynomial of two uncertain variables. The stochastic results of this case showed that the uncertainty in the long time averaged v-velocity was maximum at the region directly above the slot and decreased as we moved away from the center on either side. Conversely, the u-velocity variation was maximum in the region immediately adjacent to the slot and least in the region directly above the slot

exit. Although both input uncertainties were modeled as uniform uncertain variables, their interaction and propagation in the flow field was found to be highly non-linear. This proves the ability of NIPC method in estimating the uncertainty statistics in non-linear problems with fewer number of CFD simulations, making it highly cost effective. It was also found that the discrepancy between the experimentally measured values and the CFD simulations was very high at location $x = 0, y = 0.1mm$ above the slot. This could not be explained even with a relatively large uncertainty ($\pm 5\%$ change from the mean values) introduced in the input parameters (amplitude and frequency). Hence it can be concluded that this discrepancy may be due to the other uncertainty sources in CFD (e.g., turbulence modeling and boundary conditions) and/or uncertainties in the measurements.

5.2. FUTURE WORK

Overall, the results obtained in this study showed the potential of Non-Intrusive Polynomial Chaos as an effective uncertainty quantification method for computationally expensive high-fidelity CFD simulations applied to the stochastic modeling of synthetic jet flow fields. Future work will include the investigation of the other uncertainty sources such as geometric uncertainties and turbulence modeling parameters (such as model coefficients and wall functions), for the same test case studied in this paper. In addition, the future work will include the consideration of synthetic jet cases with cross-flow, which will focus on the uncertainty sources associated with both the main flow and the cavity region actuating the synthetic jet. The current study focused primarily on quantifying the effects of input uncertainty on the long-time averaged velocity profiles in the flow field. Our future work will include the evaluation of the effects of input uncertainties on higher order statistics like u_{rms}, v_{rms} and Reynold stresses.

In the current study linear global sensitivity analysis has be performed to evaluate the relative importance of each of the input uncertainties on the output parameter. Future work will include non-linear sensitivity analysis. Sobol indices will be calculated to determine higher-order correlation between the input and the output as well as the estimation of the effects due to mixed contributions of the input variables.

It is hoped that the uncertainty quantification results obtained for various synthetic jet cases will help the researchers to understand the effect of different uncertainty sources on the performance of the synthetic jet actuators. Efforts will be focused towards integrating the uncertainty quantification methodology into a design framework that will help in the design of robust and reliable synthetic jet actuators.

APPENDIX A

RESULTS FROM CFDVal2004 WORKSHOP

Appendix A compares the long-time averaged u and v-velocity profiles from the CFDVal2004 workshop with the base-line CFD results in this study. The CFDVal2004 workshop had invited researchers to submit their results for the test case that they had conducted experiments on. The Figure A shows the four different locations in the flow field where the velocity profiles were compared.

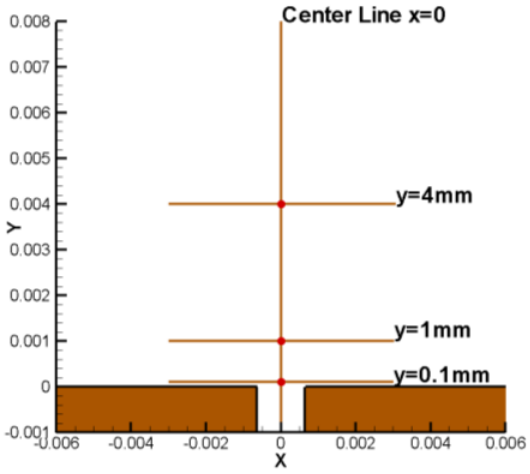

Figure A.1. Locations in the flow field where the velocity profiles were compared

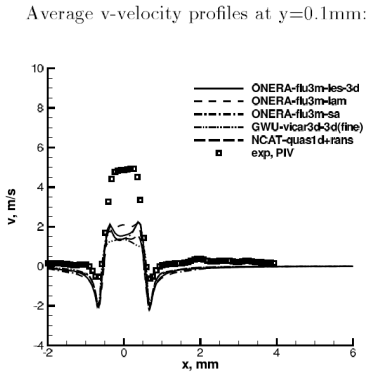

(a) v-velocity profile at $y = 0.1mm$

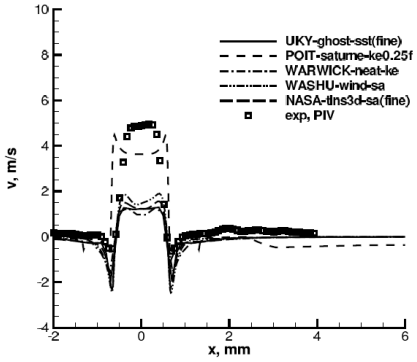

(b) v-velocity profile at $y = 0.1mm$

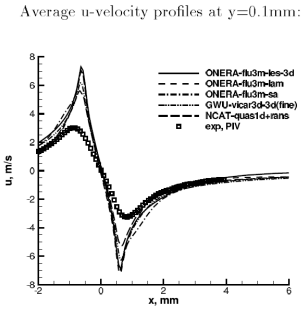

(c) u-velocity profile at $y = 0.1mm$

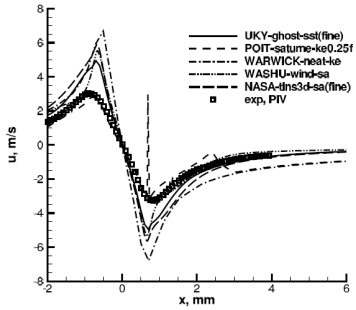

(d) u-velocity profile at $y = 0.1mm$

Figure A.2. CFDVal2004 workshop results long time averaged u and v-velocity profiles at $y = 0.1mm$ line

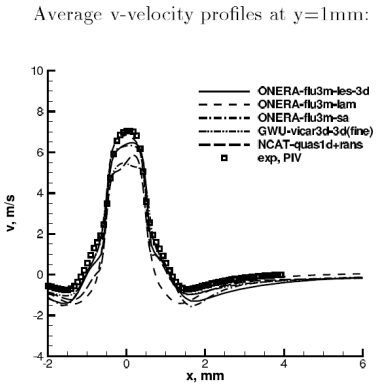

(a) v-velocity profile at $y = 1mm$

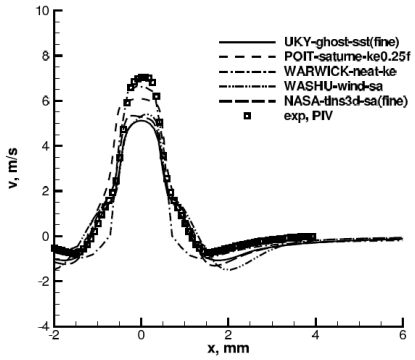

(b) v-velocity profile at $y = 1mm$

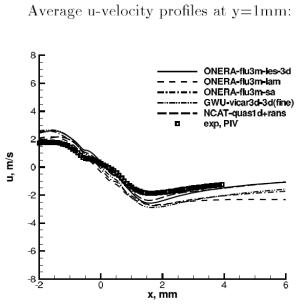

(c) u-velocity profile at $y = 1mm$

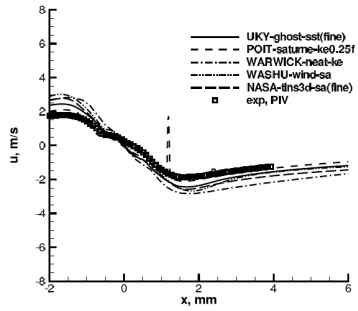

(d) u-velocity profile at $y = 1mm$

Figure A.3. CFDVal2004 workshop results long time averaged u and v-velocity profiles at $y = 1mm$ line

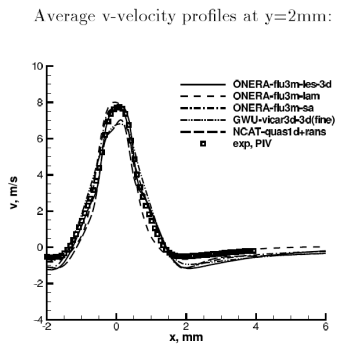

(a) v-velocity profile at $y = 2mm$

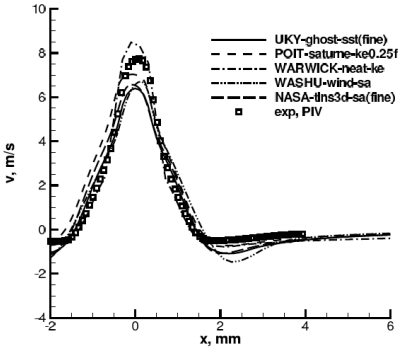

(b) v-velocity profile at $y = 2mm$

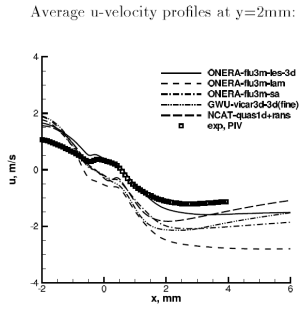

(c) u-velocity profile at $y = 2mm$

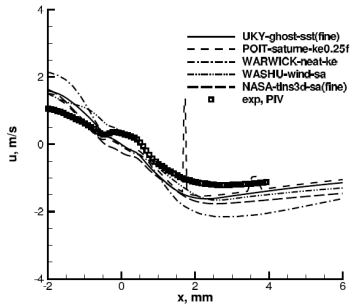

(d) u-velocity profile at $y = 2mm$

Figure A.4. CFDVal2004 workshop results long time averaged u and v-velocity profiles at $y = 2mm$ line

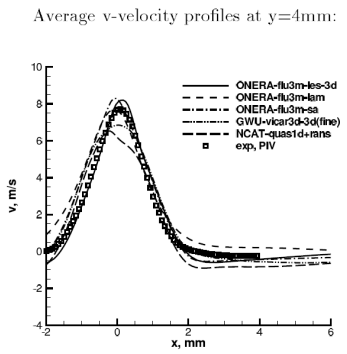

(a) v-velocity profile at $y = 4mm$

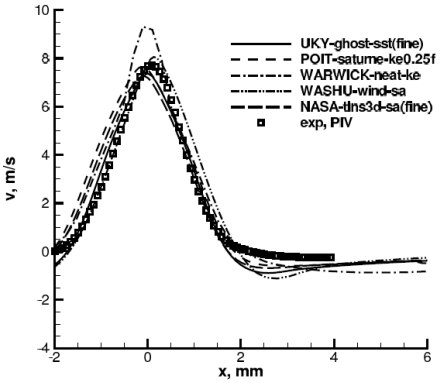

(b) v-velocity profile at $y = 4mm$

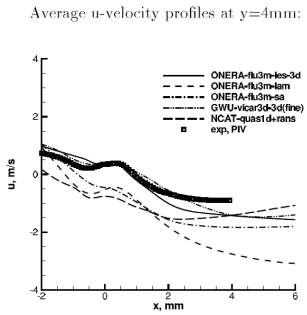

(c) u-velocity profile at $y = 4mm$

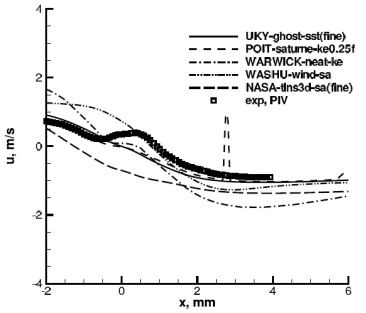

(d) u-velocity profile at $y = 4mm$

Figure A.5. CFDVal2004 workshop results long time averaged u and v-velocity profiles at $y = 4mm$ line

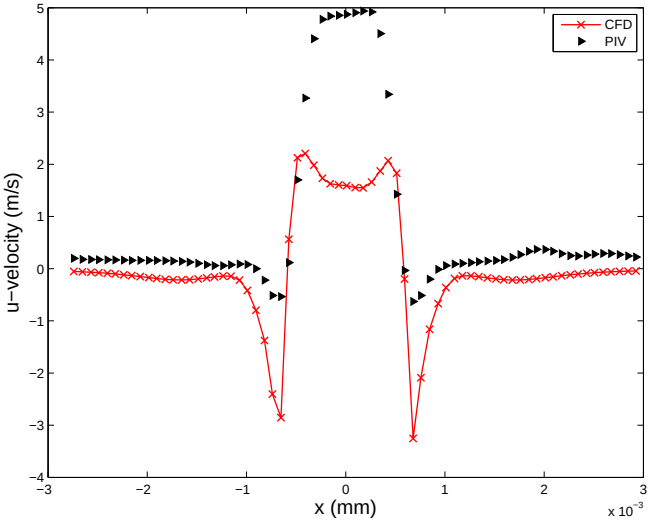

(a) Base Line v-velocity profile at $y = 0.1mm$

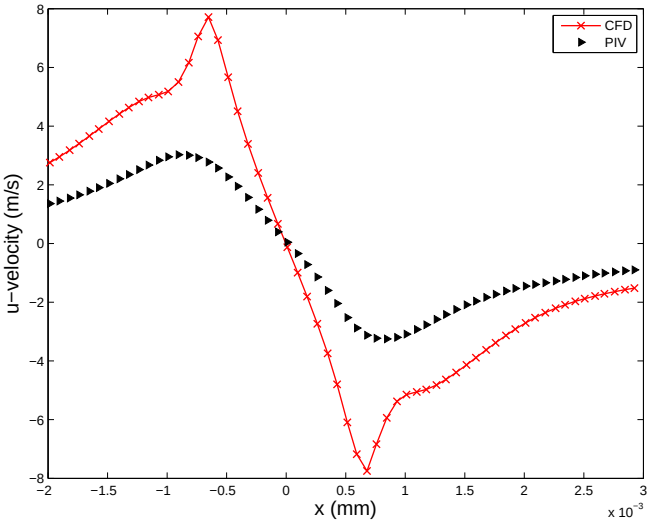

(b) Base Line u-velocity profile at $y = 0.1mm$

Figure A.6. Base Line long time averaged u and v-velocity profiles at $y = 0.1mm$ line

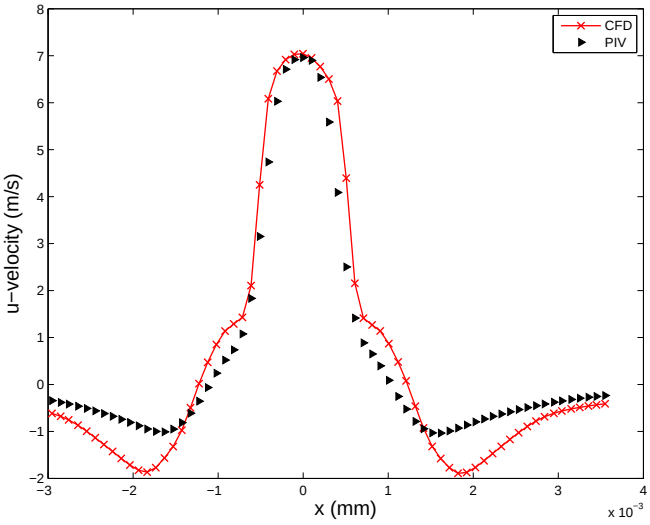

(a) Base Line v-velocity profile at $y = 1mm$

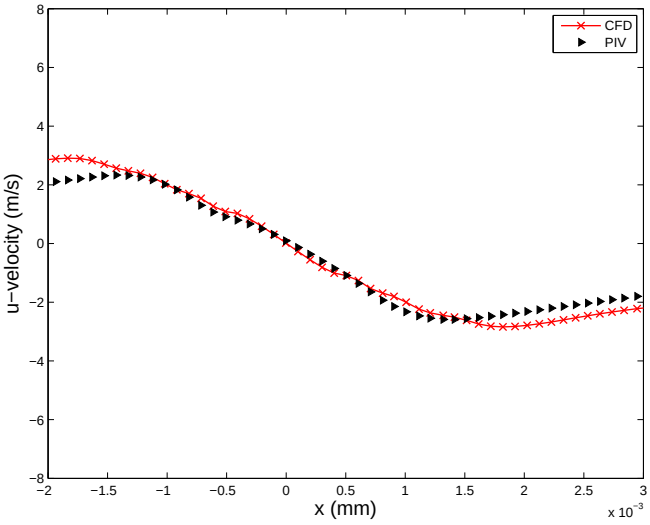

(b) Base Line u-velocity profile at $y = 1mm$

Figure A.7. Base Line long time averaged u and v-velocity profiles at $y = 1mm$ line

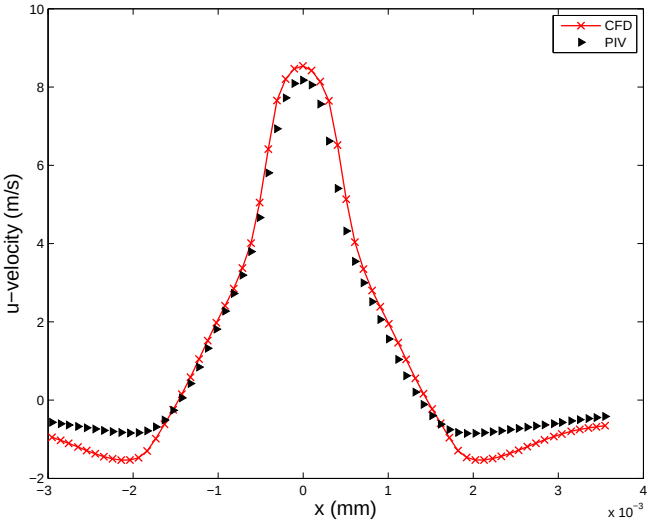

(a) Base Line v-velocity profile at $y = 2mm$

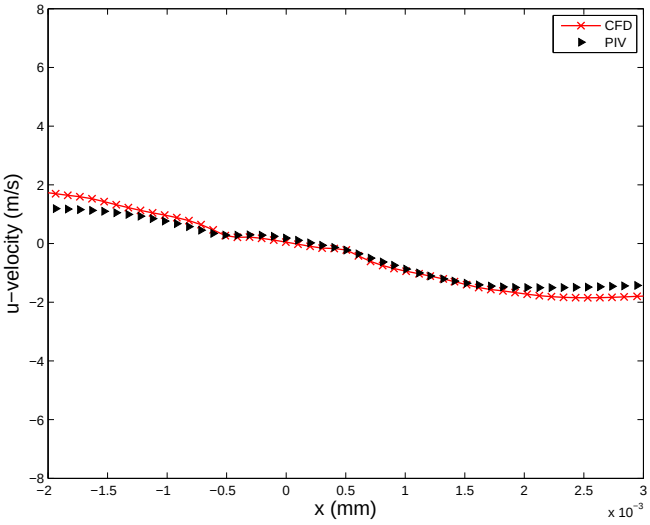

(b) Base Line u-velocity profile at $y = 2mm$

Figure A.8. Base Line long time averaged u and v-velocity profiles at $y = 2mm$ line

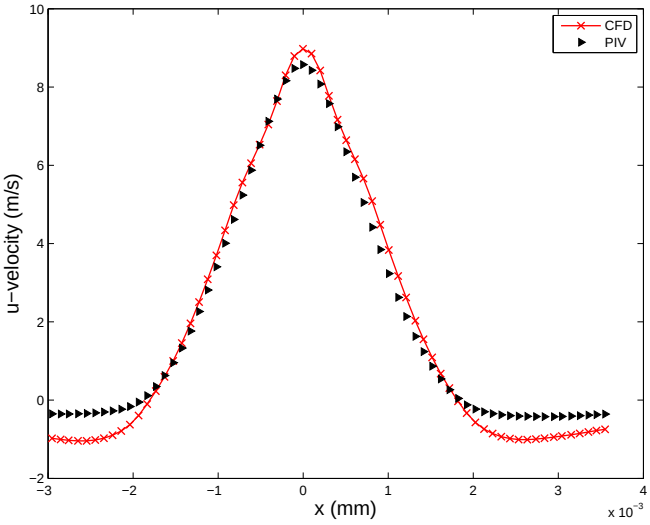

(a) Base Line v-velocity profile at $y = 4mm$

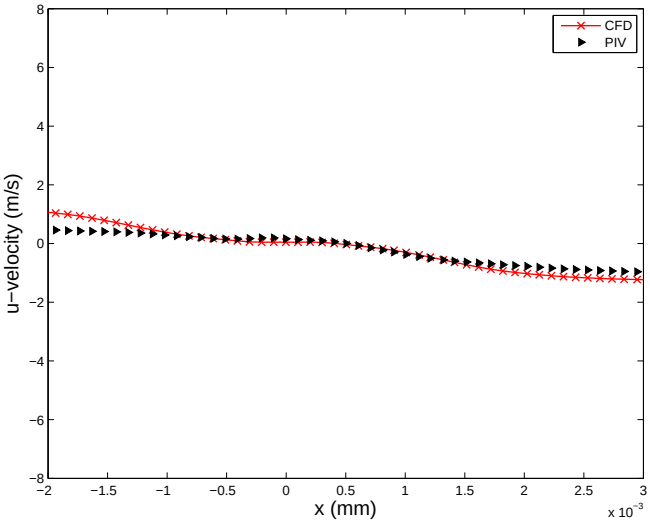

(b) Base Line u-velocity profile at $y = 4mm$

Figure A.9. Base Line long time averaged u and v-velocity profiles at $y = 4mm$ line

APPENDIX B

MATLAB CODES

Appendix B lists the MATLAB and PYTHON routines that were used in this study. The MATLAB code that implements the FDB model solves for the set of non-linear ODEs that forms the synthetic jet actuator model to give the internal pressure, exit plane velocity and the membrane displacement of the synthetic jet actuator.

The uncertainty quantification routine is written in PYTHON and is listed here. This code generates the the legender basis functions based on the order of the polynomial, reads in the long-time averaged velocity profiles obtained from FLUENT and uses the least square approach to solve for the coefficients of the polynomials. The uncertainty statistics are then extracted from these coefficients.

Fluid-Dynamics-Based Model Implementation in Matlab

```
%Author: Srikanth Adya
%Synthetic Jet Actuator Model Equation Solver
%Solves the coupled ODEs of a Synthetic Jet Flow Formulation for
%internal pressure, orifice flow velocity and membrane displacement

function X=model(fre,Amp)

%%%%%%%%%%%%%%%%%%%%%% SECTION ONE %%%%%%%%%%%%%%%%%%%%%%%%%%%%%%%%
Cleff=0.78;                                  %Effective Loss Coefficient
CI=0.705;                                    %Inertia Coefficient
dw=0.0235;                                   %Brass Shim Diameter
Aw=pi*dw^2/4;                                %Wall Area
A0=pi*0.00165^2/4;                           %Orfice Area
l0=0.00165+CI*sqrt(A0);                      %Orifice Length
P0=101325;                                   %Ambient Pressure
V0=2.50e-6;                                  %Nominal Cavity Volume
gama=1.4;                                    %Specific Heat Ratio
Us=343.0;                                    %Speed of Sound
f=fre;%100:50:3000;                          %Frequency
fw=2114;                                     %Diaphragn/Wall Natural Frequency
fh=977;                                      %Hemholtz Frequency
F=Amp;%0.574;                                %Force
cw=0.03;                                     %Damping Coefficient from LEM
```

```
kw=1.8831e+005;                                    %Diaphragm Stiffness
mw=(8700*pi*0.0235^2*0.0002/4)+(7700*pi*0.0205^2*0.00011/4);
                                                   %Diaphragm/wall mass
mwt=kw/(2*pi*fw)^2;

%%%%%%%%%%%%%%%%%%%%%%%% SECTION TWO%%%%%%%%%%%%%%%%%%%%%%%%%%%%%%%%

%This uses the built in ODE45 solver to solve the coupled ODEs by %
%calling the odetest function sequentially untill the required %%%%
%tolerance level is achieved for integration over the specified time

for i=1%:59
    omegah=Us*sqrt(A0/(10*V0));
    ma=1.225*Aw*Us/(2*pi*f(i))*(4/pi)*((2*pi*f(i)*dw/Us)/3-(2*pi*...
        f(i)*dw/Us)^3/(9*5)+(2*pi*f(i)*dw/Us)^5/(3^2*5^2*7)-(2*pi*...
        f(i)*dw/Us)^7/(3^2*5^2*7^2*9))+(2*pi*f(i)*dw/Us)^9/(3^2*5^...
        2*7^2*9^2*11);                             %added diaphragm/wall mass
    ca=1.255*Aw*Us*((2*pi*f(i)*dw/Us)^2/(2*4)-(2*pi*f(i)*dw/Us)^4/...
       (2*4^2*6)+(2*pi*f(i)*dw/Us)^6/(2*4^2*6^2*8));
                                   %added diaphragm damping coefficient
    cwt=cw+ca;
    dt=(1/(f(i)*1000));
    cycles=20;
    tspan=0:dt:cycles*(1/f(i));

    x0=[0 0 0 0 0 0];                              %Initial Conditions

    [t,x]=ode45(@odetest,tspan,x0,[],Aw,A0,Cleff,l0,P0,V0,omegah,...
            gama,F,mwt,cwt,kw,fw,f(i));
    count=1;
    for k=1000*(cycles-1):1000*cycles
        y(count,1)=x(k,3);
        y(count,2)=x(k,1);
        y(count,3)=x(k,5);
```

```
        count=count+1;
    end
    X(i)=max(y(:,1));
    Y(i)=max(y(:,2));
    Z(i)=max(y(:,3));
end

%%%%%%%%%%%%%%%%%%%%%%%%%% SECTION THREE %%%%%%%%%%%%%%%%%%%%%%%%%%

%This section converts the second order ODEs into first order and puts
%it in a form suitable of the ODE45 solver. The three model equations
%results into six first order ODEs one each for internal pressure, %%%
%internal pressure gradient, orifice velocity, orifice velocity %%%%%
%gradient, diaphragm displacement and diaphragm velocity %%%%%%%%%%%

function xprime=odetest(t,x,Aw,A0,Cleff,l0,P0,V0,omegah,gama,F,mwt,cwt,
                        kw,fw,f)
% Since the states are passed in as a single vector, let
% x(1) = p
% x(2) = p'
% x(3) = u
% x(4) = u'
% x(5) = x
% x(6) = x'
xprime(5,1)= x(6);
xprime(6,1)= (F*sin(2*pi*f*t)/mwt)-(x(1)*Aw/mwt)-2*0.03*2*pi*fw*x(6)...
             -(2*pi*fw)^2*x(5);                    %Membrane Dynamics

xprime(1,1)= x(2);
xprime(2,1)= -((V0*Cleff)/(2*gama*A0*P0*l0))*abs(x(2)-(gama*Aw*P0*...
             x(6)/V0))*(x(2)-(gama*Aw*P0*x(6)/V0))-omegah^2*x(1)+...
             (gama*Aw*P0/V0*((F*sin(2*pi*f*t)/mwt)-(x(1)*Aw/mwt)-...
             2*0.03*2*pi*fw*x(6)-(2*pi*fw)^2*x(5)));
                                    %Dynamic Internal Pressure
```

```
xprime(3,1)= x(4);
xprime(4,1)= -(Cleff/10)*abs(x(3))*x(4) - omegah^2*x(3)+(Aw/A0)*...
                omegah^2*x(6);                    %Orifice Flow Velocity
```

model.m

Uncertainty Quantification Routine in Python

```
from sympy import *
import sympy
from numpy import *
import math
import numpy
import Gaussian_Intergration
#ifile = open("LHSample5.txt",'r')
f=open('output_model_problem_NIPC.txt','r')
f=f.readlines()
Mean=[]
std=[]
for l in range(5):
    T=[3,6,10,15,21,28]
    P=T[l]
    p=P*2
    alpha=numpy.zeros([p,1])
    a=[]
    b=[]
    for i in range(p):
        dummy=f[i].split()
        alpha[i][0]=dummy[2]
        a.append(dummy[0])
        b.append(dummy[1])

    A=[]
    B=[]
    C=[]
    si=numpy.zeros([p,P])
    x=Symbol('x')
```

```
y=Symbol('y')
for i in range(7):
    A.append(legendre(i,x))
for i in range(7):
    B.append(legendre(i,y))
#first order expansion
count=0
C.append(A[0]*B[count])
for i in range(1,-1,-1):
    C.append(A[i]*B[count])
    count+=1
#second order expansion
count=0
for i in range(2,-1,-1):
    C.append(A[i]*B[count])
    count+=1
#third order expansion
count=0
for i in range(3,-1,-1):
    C.append(A[i]*B[count])
    count+=1
#fourth order expansion
count=0
for i in range(4,-1,-1):
    C.append(A[i]*B[count])
    count+=1
##fifth order expansion
count=0
for i in range(5,-1,-1):
    C.append(A[i]*B[count])
    count+=1
##sixth order expansion
count=0
for i in range(6,-1,-1):
    C.append(A[i]*B[count])
```

```
        count+=1

    for i in range(P):
        for j in range(p):
            si[j][i]=C[i].subs(x,a[j]).subs(y,b[j]).evalf()

    #Solving for the coefficients#
    c,resid,rank,s=linalg.lstsq(si,alpha)

    #Computing Standard Deviation
    variance=numpy.zeros([1,1])
    for i in range(1):
        dummy=c[:,i]
        for k in range(1,P):#P
            inner_product=C[k]*C[k]
            X=Gaussian_Intergration.gauss_quad_Int(inner_product)
            X=Gaussian_Intergration.gauss_quad_Int(X)
            variance[i][0]=variance[i][0]+ 0.25*X*dummy[k]**2
    Mean.append(c[0,0])
    dummy=sqrt(variance[i][0])
    std.append(dummy)
    string=str('coe_model_')+str(l)+str('.txt')
    coe=open(string,'w')
    for i in range(P):
        coe.write(str(c[i,0])+'\n')
    coe.close()
```

legendre_UQ.py

APPENDIX C

COMPUTATIONAL MODELING CASE SETUP PROCEDURE

Grid Generation

The grid for this case was taken from CFDVal2004 workshop website hence the geometry and the mesh was already readily available. The mesh on the website was in PLOT3D format. GAMBIT

Fluent Case Setup

For the purpose of parallel processing, the cases were run on a high performance computing cluster. The following sub-section describes the procedure to launch a parallel FLUENT job on the cluster using multiple nodes.

Launching Parallel FLUENT

FLUENT can be launched either interactively or can be submitted as a job on the cluster. To run a parallel FLUENT application interactively an interactive session must first be requested using a PBS scheduler. The following is an example for requesting multiple nodes tor interactive FLUENT processing:

qsub -I -X -l nodes=8:ppn=2 -l walltime=50:00:00 -q hos_cpu@nic-cluster.mst.edu

This will assign 16 processors for a wall time of 50hours on hos_cpu nodes that are dedicated to Computational Fluid Dynamics and Aerospace Research Lab. It can take a couple of minutes before the requested nodes become available. Once the nodes are assigned to the requested job, FLUENT can be launched for interactive parallel processing using the following command line

fluent 2ddp -t16 -pethernet -cnf=$PBS_NODEFILE -g -ssh /nethome/users/username/path_to_fluent_file

Alternatively FLUENT case can also be submitted as a job. A typical job file is as follows:

#/bin/bash

#PBS -q hos_cpu@nic-cluster.mst.edu

#PBS -m abe

#PBS -M username@mst.edu

```
#PBS -l nodes=8
#PBS -l walltime=50:00:00
#PBS -d /nethome/users/username
fluent 2ddp -t8 -pethernet -cnf=$PBS_NODEFILE -g -ssh /nethome/users/username/fluent_command_file
```

The above job file needs a command file that tells FLUENT to run the desired case. The command file for an unsteady case looks like below:

```
/file/rcd /nethome/users/username/casefile.cas
/file/autosave/data-frequency 50
/solve/set/time-step 0.0000022487
/solve/dual-time-iterate
15000
15
/file/wd /nethome/users/username/datafile.dat
/exit
```

Solver Settings

The following snapshots illustrate the step by step procedure to set up the solver.

Step 1: A pressure based solver was selected. Since the membrane motion is time dependent, the solver type was set to transient. Velocity formulation was set as absolute and planar 2D space option was selected.
Step 2: Once the grid was fully setup in GAMBIT, the mesh file was imported into FLUENT. Grid check (Mesh> Check) was performed to ensure that there are no negative volumes or skewed cells.

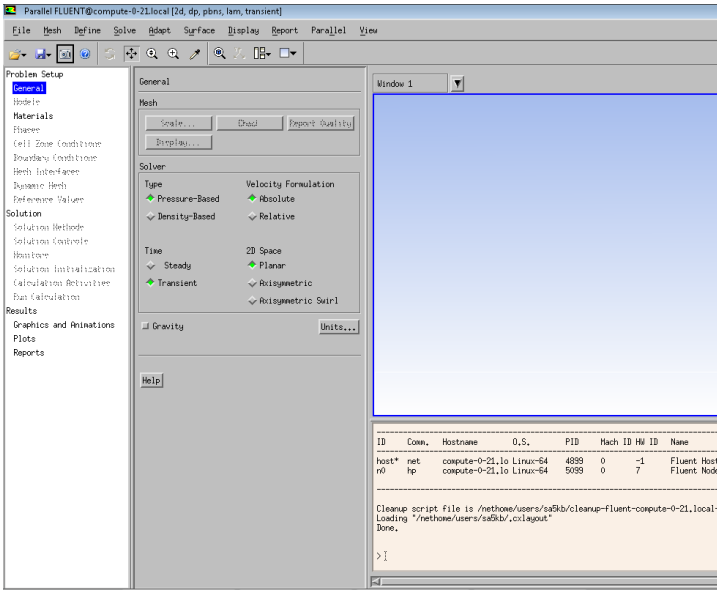

(a) Case setup Step 1

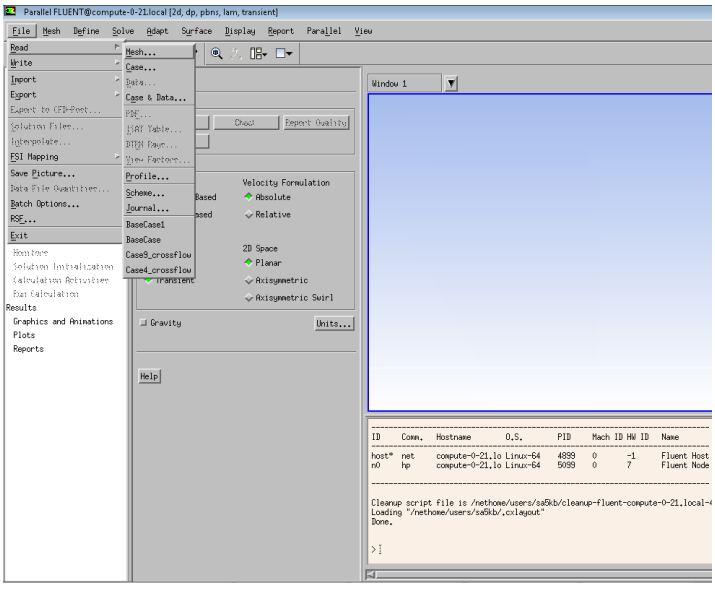

(b) Case setup Step 2

Step 3: The two equation Menter SST k-omega turbulence model was selected (Define> Models) to solve the RANS equations.
Step 4: The material properties for air (working fluid) was updated based on CFDVal2004 workshop inputs.

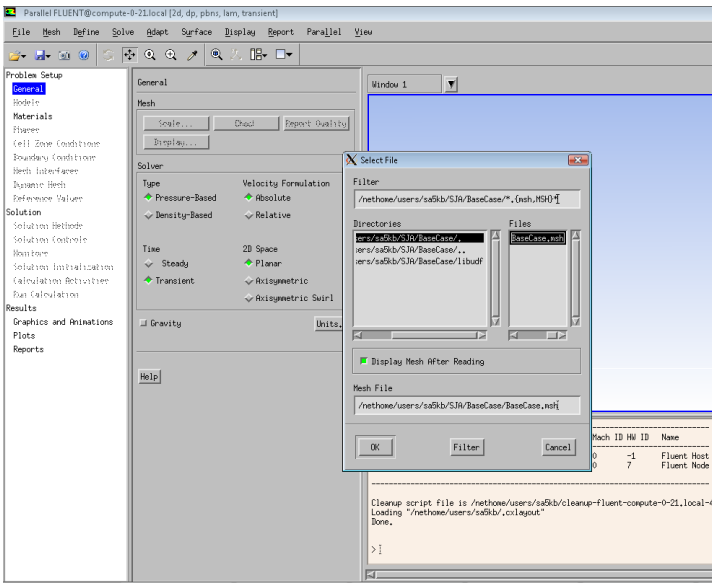

(c) Case setup Step 3

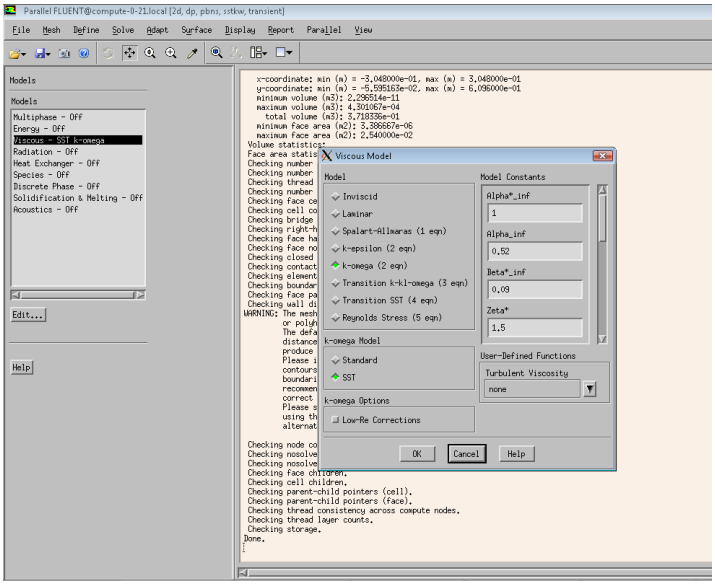

(d) Case setup Step 4

Step 5: Next, boundary conditions were assigned to the boundaries of the mesh. The left and right side of the cavity except the membrane were assigned as wall.
Step 6: The aluminum plate was assigned as wall.

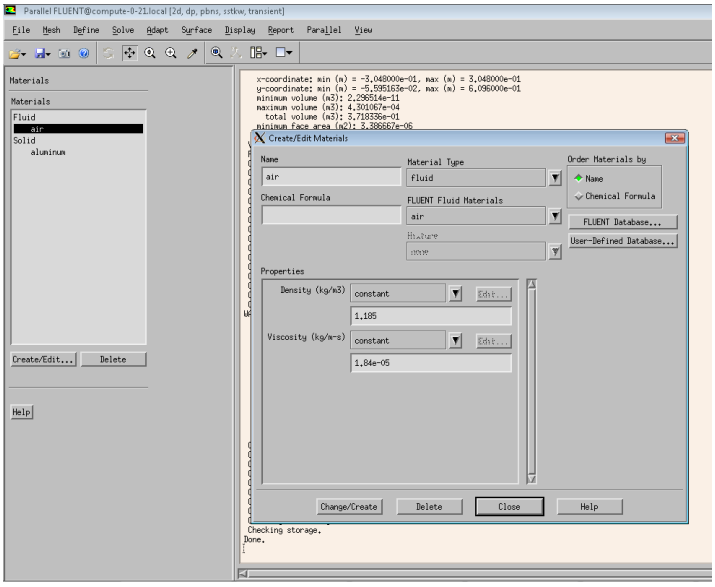

(e) Case setup Step 5

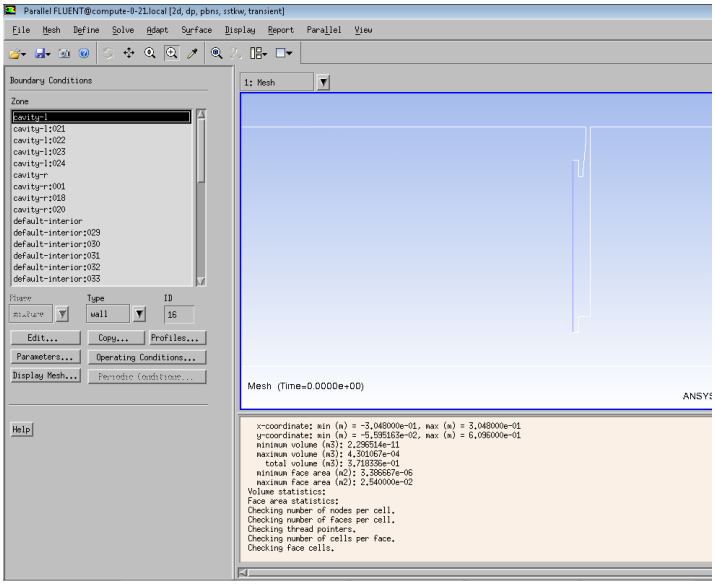

(f) Case setup Step 6

Step 7: The left, right and top boundaries of the outflow domain were assigned outflow boundary condition.

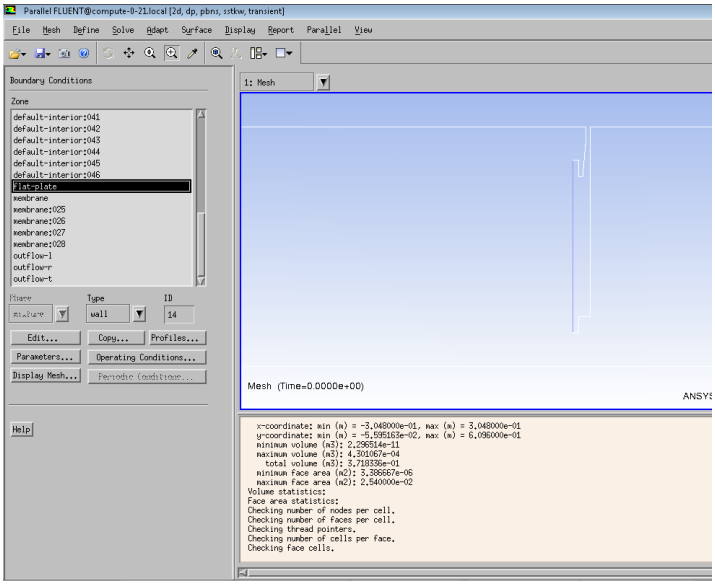

(g) Case setup Step 7

Step 8: The oscillating membrane on the left side of the cavity has a time dependent motion. To simulate this motion the membrane was assigned a time dependent velocity inlet boundary condition. This was done using a user defined function. A UDF was written in C and was compiled using Define>User defined>Functions>Compiled. Here it should be noted that while assigning the libudf directory name, the complete path to the directory has to be mentioned for FLUENT to successfully compile the C file and build the libudf directory. Once the program is compiled successfully it was loaded to the solver by clicking on load.
Step 9: All the elements of the membrane were assigned the time dependent udf defined velocity profile.

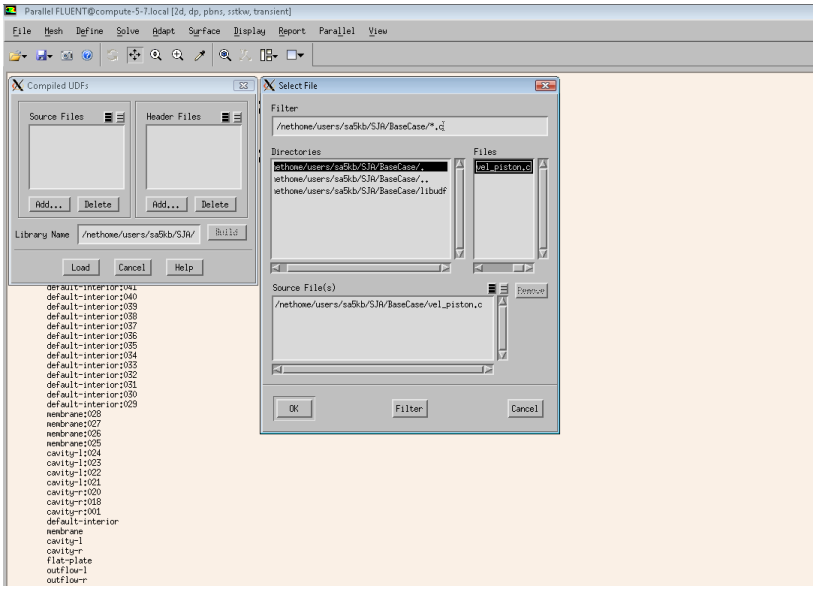

(h) Case setup Step 8

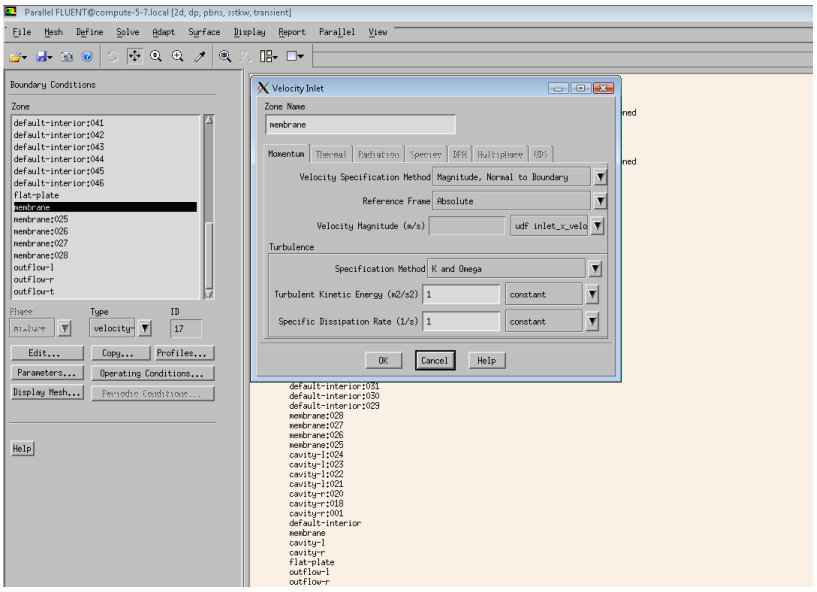

(i) Case setup Step 9

Step 10: The residual monitor for continuity equation was set at 10e6(Solve>Monitors>Residual).

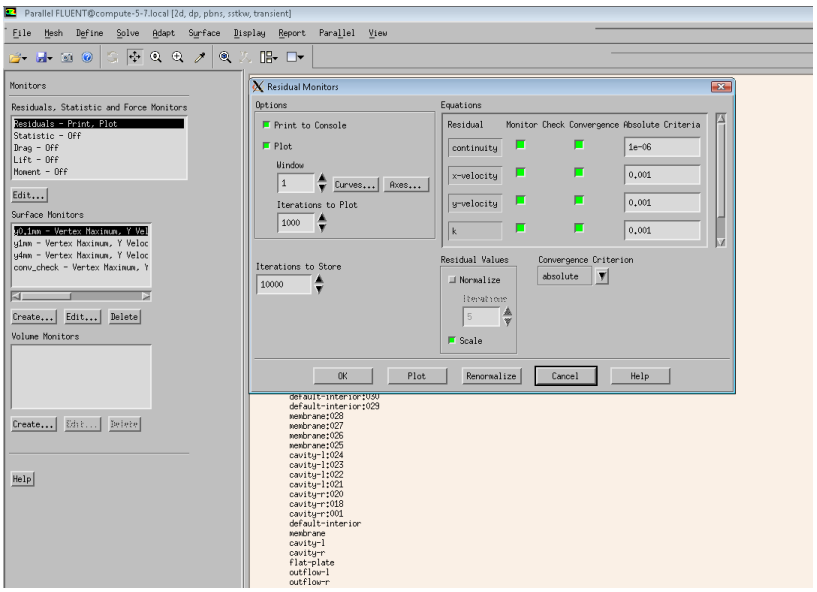

(j) Case setup Step 10

Step 11: Points and lines were created in the flow field were the convergence had to be monitored.
Step 12: To monitor the convergence of the solution, surface monitors were initialized at the points and lines created in the previous step(Solve>Monitors>Surface Monitors).

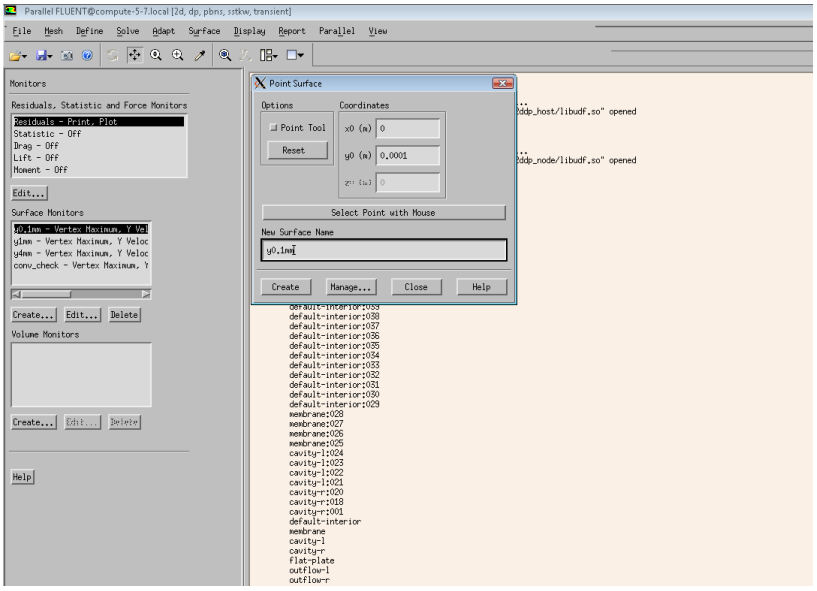

(k) Case setup Step 11

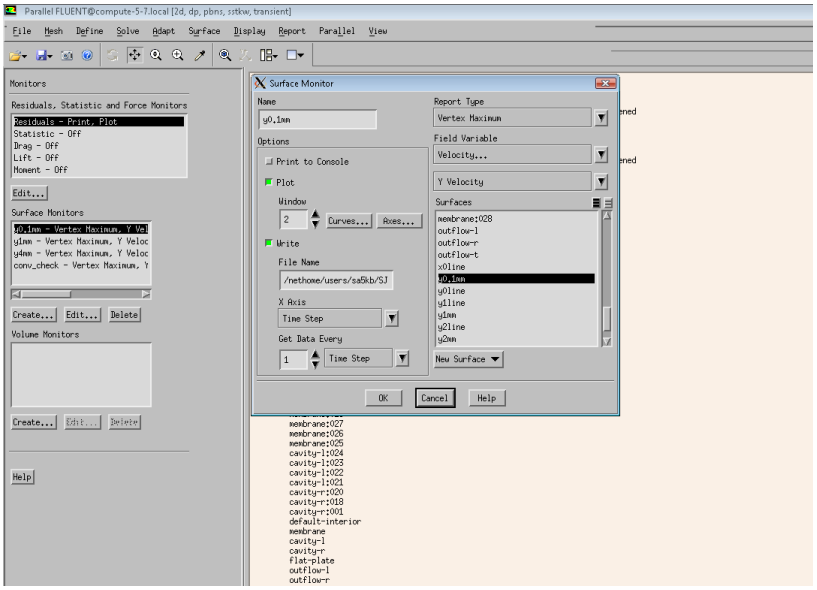

(l) Case setup Step 12

Step 13: Solution was initialized by assigning the initial values to all the zones.
Step 14: Data was saved at every 50 iterations. The time step size and number of iterations per time step were assigned and the solution was allowed to run for the desired number of cycles(Solve>Run Calculations).

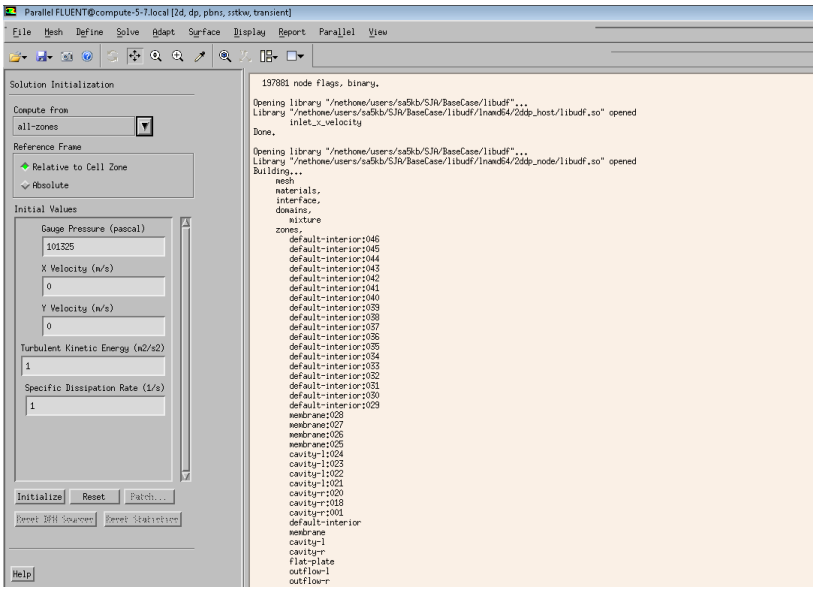

(m) Case setup Step 13

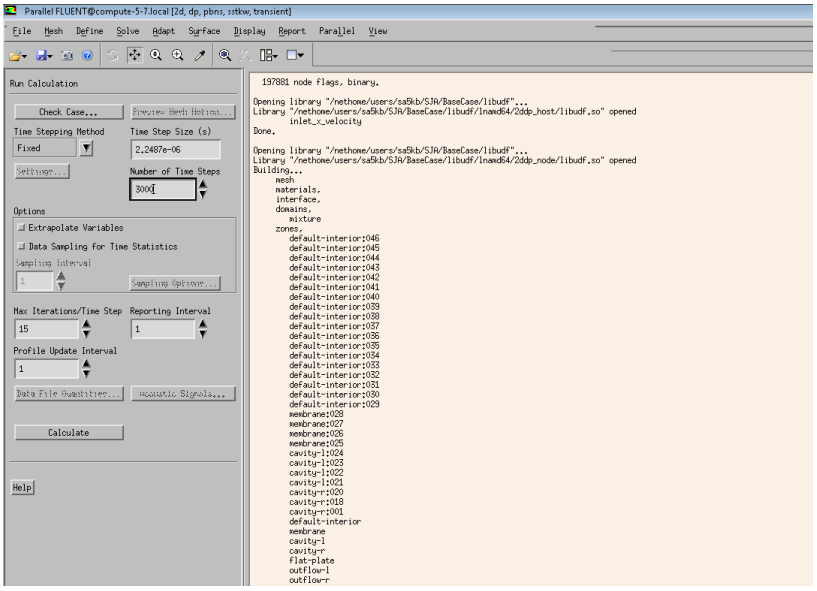

(n) Case setup Step 14

BIBLIOGRAPHY

[1] Mohamed Gad el Hak. *Flow Control,Passive Active and Reactive Flow Management*. Cambridge University Press, 1 edition, 2000.

[2] Glezer A. and Amitay M. Synthetic jets. *Annual Review of Fluid Mechanics*, 34:503–529, 2002.

[3] and Miguel R. Visbal Donald P. Rizzetta and Michael J. Stanek. Numerical investigation of synthetic-jet flow fields. *AIAA*, 37(8), August 1999.

[4] R.Mittal and P.Rampunggoon. Interaction of a synthetic jet with a flat plate boundary layer, aiaa 2001-2773. *AIAA*, August 2001.

[5] J. Cui, Agarwal R.K, and Cary A.W. Numerical simulation of the interaction of the synthetic jet with a turbulent boundary layer, aiaa paper 2003-3458. June, 2003.

[6] Rumsey C. L. Proceedings of the 2004 workshop on cfd validation of synthetic jets and turbulence seperation control. 2004.

[7] Rumsey C. L., Sellers W. L., Vatsa V. N., and Viken S. A. Summary of the 2004 computational fluid dynamics validation workshop on synthetic jets. *AIAA Journal*, 44(2):194–207, February-2006.

[8] Rumsey C. L. Successes and challenges for flow control simulations. *International Journal of Flow Control*, 1(1):1–27, March-2009.

[9] D. Lucor, J. Meyers, and P. Saugat. Sensitivity analysis of large-eddy simulations to subgrid-scale-model parametric uncertainty. *Journal of Fluid Mechanics*, 585:255–279, 2007.

[10] H. N. Najm. Uncertainty quantification and polynomial chaos techniques in computational fluid dynamics. *Annual Review of Fluid Mechanics*, 41:35–52, 2009.

[11] S. Hosder and R. W. Walters. Non-intrusive polynomial chaos methods for uncertainty quantification in fluid dynamics, AIAA-paper 2010-0129. In 48^{th} *AIAA Aerospace Sciences Meeting*, Orlando, FL, January 4-7, 2010.

[12] S. Hosder, Walters R. W., and M. Balch. Point-collocation nonintrusive polynomial chaos method for stochastic computational fluid dynamics. *AIAA Journal*, 48(12), December 2010.

[13] W. L. Oberkampf, J.C. Helton, and K. Sentz. Mathematical representation of uncertainty, aiaa-paper 2001-1645. In 3^{rd} *Non-Deterministic Approaches Forum, Seattle, WA*, April 2001.

[14] Hosder S., Walters R., and Perez. A non-intrusive polynomial chaos method for uncertainty propagation in CFD simulations. 2006.

[15] N. Wiener. The homogeneous chaos. *American Journal of Mathematics*, 60(4):897–936, 1938.

[16] D. Xiu and G. E. Karniadakis. Modeling uncertainty in flow simulations via generalized polynomial chaos. *Journal of Computational Physics*, 187(1):137–167, May, 2003.

[17] M. S. Eldred, C. G. Webster, and P. G. Constantine. Evaluation of non-intrusive approaches for wiener-askey generalized polynomial chaos, AIAA-paper 2008-1892. In 10^{th} *AIAA Non-Deterministic Approaches Forum*, Schaumburg, IL, April, 2008.

[18] R. W. Walters and L. Huyse. Uncertainty analysis for fluid mechanics with applications. Technical report, ICASE 2002-1, NASA/CR-2002-211449, NASA Langley Research Center, Hampton, VA, 2002.

[19] S. Hosder, R. W. Walters, and M. Balch. Efficient sampling for non-intrusive polynomial chaos applications with multiple input uncertain variables, AIAA-paper 2007-1939. In 9^{th} *AIAA Non-Dterministic Approaches Conference*, Honolulu, HI, April, 2007.

[20] S. Hosder and L. Maddalena. Non-intrusive polynomial chaos for the stochastic cfd study of a supersonic pressure probe, AIAA-paper 2009-1129. In 9^{th} *AIAA Non-Dterministic Approaches Conference*, Honolulu, HI, April, 2007.

[21] Benjamin R. Bettis and Serhat Hosder. Quantification of uncertainty in aerodynamic heating of a reentry vehicle due to uncertain wall and freestream conditions. In 10^{th} *AIAA/ASME Joint Thermophysics and Heat Transfer Conference, Chicago, Illinois.*

[22] Toshikazu Nishida Mark Shelpak and Louis Cattafesta Quentin Gallas, Ryan Holman. Lumped element modeling of piezoelectric-drien synthetic jet actuator. *AIAA Journal*, 41(2), February 2003.

[23] R.N Sharma. An analytical model for synthetic jet actuation,AIAA-paper 2006-3035. In 3^{rd} *AIAA Flow Control Conference*, San Francisco, CA, June, 2006.

[24] R.N Sharma. Some insights into synthetic jet actuation from analytical modeling. In 16^{th} *Australian Fluid Mechanics Conference*, December, 2006.

[25] R.N Sharma. Fluid-dynamics-based analytical model for synthetic jet actuation. *AIAA Journal*, 45(8), 2007.

[26] Suryanarayana A.N. Prasad, Bhavani V. Sankar, Louis N. Cattafestaand Stephen Horowitz, Quentin Gallas, and Mark Sheplak. Two-port electroacoustic model of an axisymmetric piezoelectric composite plate. In 43^{rd} *AIAA/ASME/ASCE/AHS/ASC Structures, Structural Dynamics, and Materials Conference 22-25 April 2002 / Denver, Colorado*, 2002.

[27] John D. Anderson Jr. *Computational Fluid Dynamics: The Basics with Applications.* McGraw-Hill.

[28] Menter F. R. Two-equation eddy-viscosity turbulence models for engineering applications. *AIAA Journal*, 32(8):1598–1605, October-December 2006.

[29] Fluent technical manual. *Ansys, Inc.*

[30] Langley research center workshop cfd validation of synthetic jets and turbulent separation control website, http://cfdval2004.larc.nasa.gov/.

VITA

Srikanth Adya was born in Bangalore, India, on March 1, 1985. He got his Bachelor of Engineering degree in Mechanical Engineering from Vishweshwaraiah Technological University in 2006. He later worked as a Design Engineer in Schneider Electric where he was involved in the design of electro-mechanical switch gear for low voltage applications. He started his graduate studies at Missouri University of Science and Technology and joined Dr. Serhat Hosder as a Research Assistant. He graduated in May of 2011 with a Master of Science in Aerospace Engineering. His area of focus being Computational Fluid Dynamics, Flow Control and Uncertainty Quantification.